© 2017 Krishna Vasanth Valavala

THERMOELECTRIC CHARACTERIZATION OF ONE- AND TWO-DIMENSIONAL MATERIALS

BY

KRISHNA VASANTH VALAVALA

DISSERTATION

Submitted in partial fulfillment of the requirements
for the degree of Doctor of Philosophy in Mechanical Engineering
in the Graduate College of the
University of Illinois at Urbana-Champaign, 2017

Urbana, Illinois

Doctoral Committee:

Professor Sanjiv Sinha, Chair and Director of Research
Professor Placid Ferreira
Professor Xiuling Li
Professor Arend van der Zande

# ABSTRACT

Thermoelectric materials are useful for a wide range of applications like waste heat removal, solid state cooling, and power generation in space missions etc. A material's thermoelectric figure of merit ($zT$), which determines its performance in the applications listed above, depends on its Seebeck coefficient ($S$), electrical conductivity ($\sigma$) and thermal conductivity ($\kappa$) as $zT = S^2\sigma T/\kappa$. Low dimensional materials like nanowires (1D) or atomically thin films (2D) are promising as they exhibit lower thermal conductivities or higher power factors ($S^2\sigma$) compared to their bulk (3D) counterparts. The thermal and electrical properties of these low dimensional materials could be further tuned by modifying their microstructure to achieve higher $zT$s. To achieve such material tuning in a controlled fashion, it is necessary to understand the physical mechanisms that govern the relationships between a material's microstructure and its thermoelectric properties. Reliable experimental techniques and proper interpretation of the experimental results are essential to gain insights into the physical mechanisms of interest.

This dissertation addresses the characterization of thermoelectric properties of one- and two-dimensional materials with the goal of studying the governing physical mechanisms. An experimental study on the Seebeck coefficient and electrical conductivity of atomically thin Molybdenum disulphide ($MoS_2$), a two dimensional semiconducting material, is presented. Seebeck coefficient and electrical conductivity are electronic transport properties. In $MoS_2$ and other two dimensional materials, the electron transport is heavily influenced by the localized states formed in their band gaps. Using the experimentally obtained temperature and gate voltage dependence of $S$ and $\sigma$ and a theoretical model, a determination of the nature of the localized states and the electron transport mechanism is made.

For the one dimensional materials, the focus is on the measurement of their thermal conductivity. Most of the advances in the figure of merit were

achieved in the recent past by reducing the thermal conductivity. In this light, the understanding of phonon transport in the low dimensional materials gains importance. A suspended bridge measurement platform is a very commonly used technique to measure thermal conductivity of one-dimensional materials. This technique is very useful for studying the underlying fundamental transport physics as it allows measurement on an individual 1D structure, as opposed to $3\omega$ and TDTR methods which can only measure an assembly of 1D materials. Combining this measurement technique with precise microstructure characterization using transmission electron microscopy (TEM), the influence of the microstructure on thermal transport can be deducted. In a study done previously on silicon nanowires, different but similarly made 1D structures were used for microstructure characterization and thermal measurement. This mismatch introduces an uncertainty in the correlation between microstructure and the phonon transport. In this dissertation, a modification to the usual measurement platform is presented which allows TEM imaging and thermal measurement on the same 1D structure. Furthermore, refinements to the measurement principal that have been implemented in our lab to enable measurement on much finer 1D structures are discussed.

*To my parents*

# ACKNOWLEDGMENTS

Firstly, I want to express my deepest gratitude to my advisor Prof. Sanjiv Sinha for his support and guidance over the years. I want to thank him for giving me the intellectual freedom to define my dissertation topic as per my interest and curiosity. His detail oriented approach and his ability to explain complex subject matter in simple terms continue to inspire me to become a better researcher.

My sincere thanks to Prof. Placid Ferreira and Prof. Xiuling Li who provided valuable input in my preliminary exam as well as during our collaboration on the silicon nanowire thermoelectrics project. My special thanks to Prof. Arend van der Zande and his graduate student Sunphil Kim for providing me the $MoS_2$ samples for my measurements.

I consider myself extremely fortunate to have had the opportunity to work with the people in my research group. Their support and constructive criticism over the years has often helped me refine my research and my presentations. Special thanks to Jyothi swaroop Sadhu who has been my friend since high school and helped me immensely as I transitioned into graduate school. Thanks to Marc Ghossoub, Jun Ma and Hongxiang Tian for taking many classes with me, and for extending their skills and expertise to boost my research. Thanks to Dhruv, Manju and Keith for the intellectually stimulating environment they create in the group. I want to take this opportunity to remember Late. Dr. Myunghoon Seong who had been my mentor during the first few years of my stay at UIUC.

The frustrations that often accompanied my research would have been unbearable without the company of my dear friends Sahand, Laura, Danielle, Sirisha, Sara, Jan, Udit, Sushil and Nishanth.

Finally, no words can describe the love and gratitude I feel for my parents. Like every other milestone in my life, this dissertation would not have been possible without their unconditional love and unwavering support.

# TABLE OF CONTENTS


LIST OF FIGURES . . . . . . . . . . . . . . . . . . . . . . . . . . . . vii

CHAPTER 1 INTRODUCTION . . . . . . . . . . . . . . . . . . . . . . 1
- 1.1 A brief background on thermoelectrics . . . . . . . . . . . . . 1
- 1.2 Motivation . . . . . . . . . . . . . . . . . . . . . . . . . . . 4
- 1.3 Thesis structure . . . . . . . . . . . . . . . . . . . . . . . . 8

CHAPTER 2 THEORY OF THERMOELECTRIC PROPERTIES IN HOPPING REGIME . . . . . . . . . . . . . . . . . . . . . . . . 10
- 2.1 Extended and localized states . . . . . . . . . . . . . . . . . . 10
- 2.2 Semi-classical model for $S$ and $\sigma$ . . . . . . . . . . . . . . . 14
- 2.3 Miller Abrahams network and percolation theory . . . . . . . 16
- 2.4 Temperature dependence of thermoelectric properties . . . . . 22
- 2.5 Conclusion . . . . . . . . . . . . . . . . . . . . . . . . . . . 26

CHAPTER 3 EXPERIMENTAL INVESTIGATION OF THERMOELECTRIC PROPERTIES OF $MOS_2$ MONOLAYERS . . . . . 27
- 3.1 Introduction . . . . . . . . . . . . . . . . . . . . . . . . . . 27
- 3.2 Device fabrication and characterization . . . . . . . . . . . . . 28
- 3.3 Measurement principle and Instrumentation . . . . . . . . . . . 31
- 3.4 Results and Discussion . . . . . . . . . . . . . . . . . . . . . 45
- 3.5 Conclusion . . . . . . . . . . . . . . . . . . . . . . . . . . . 55

CHAPTER 4 THERMAL CONDUCTIVITY MEASUREMENT OF 1D STRUCTURES . . . . . . . . . . . . . . . . . . . . . . . . . 57
- 4.1 Introduction . . . . . . . . . . . . . . . . . . . . . . . . . . 57
- 4.2 Measurement Principle . . . . . . . . . . . . . . . . . . . . . 58
- 4.3 Limitations and solutions . . . . . . . . . . . . . . . . . . . . 61
- 4.4 Conclusions . . . . . . . . . . . . . . . . . . . . . . . . . . . 67

CHAPTER 5 CONCLUSION AND FUTURE WORK . . . . . . . . 69

REFERENCES . . . . . . . . . . . . . . . . . . . . . . . . . . . . 72

# LIST OF FIGURES

1.1 Schemtic of the thermoelectric devices for power generation(left) and for refrigeration(right). . . . . . . . . . . . . . . . . 2
1.2 Thermal conductivity of nanowires measured as a function of temperature. Low temerpature data is used to obtain the boundary scattering rates for various roughness profiles . . 5
1.3 Roughness profile of silicon nanowires obtained by stitching a series of images taken in a transmission electron microscope. 5
1.4 Semiclassical calculations of the thermoelectric properties of pristine $MoS_2$ with no localized states. Figure taken from ref [1] . . . . . . . . . . . . . . . . . . . . . . . . . . 7

2.1 Schematic representation of electrons in an $MoS_2$ crystal in equilibrium and non-equilibrium conditions. Top: Electrons distributed uniformly throughout the crystal under equilibrium conditions. Bottom: Temperature gradient results in electron concentration gradient which can be used to run an electrical load . . . . . . . . . . . . . . . . . . . . . . 11
2.2 Schematic of density of states in $MoS_2$ crystal.The dashes represent the states the electrons can populate. Conduction and valence band states are bounded by red and blue lines respectively. The states bounded by the black line are the localized states that are formed because of imperfections in the crystal . . . . . . . . . . . . . . . . . . . . . . 12
2.3 Schematic of the wavefunctions of extended (left)vs localized states (right). The wavefunctions of extended states span over the crystal and are not localized to one site. The localized sites on the other hand have wavefunctoins which die out within a few inter-atomic distances. . . . . . . . . . . . 13
2.4 Schematic of the electron transport mechanisms of exteded states (left) and loclaized states (right). . . . . . . . . . . . . . 13
2.5 Miller Abrahams network formed by bonding each pair of hopping sites with a resistance decribed by Eq. 2.11 . . . . . . 18

2.6 Schematic representation of the percolation theory method. All the bonds in the full network shown in (d) are removed and gradually reintroduced (a,b) till the percolation threshold (c) is reached. . . . . . . . . . . . . . . . . . . . . . . 20
2.7 Geometry in a composit energy-distance space encompassing possible desitnation sites $j$ availbale to bond with site $i$ under bonding criteria given by Eq.2.20 . . . . . . . . . . . . 23

3.1 Images of the $MoS_2$ device at various steps of its fabricationn process . . . . . . . . . . . . . . . . . . . . . . . . . . 29
3.2 Linear $I$ vs $V_D$ curves at different gate voltages indicating Ohmic contacts between $MoS_2$ monolayer and Ti/Pd/Au metal stack . . . . . . . . . . . . . . . . . . . . . . . . . . . 30
3.3 Typical Raman spectrum observed for the CVD grown $MoS_2$ monolayer used in this study. The black line represents the Lorentzian fit of the Raman shift data shown in red . . . . . . . . . . . . . . . . . . . . . . . . . . . . . 30
3.4 Photoluminescence spectrum observed for the CVD grown $MoS_2$ monolayer used in this study . . . . . . . . . . . . . . . . 31
3.5 Schematic of the device fabricated for the measurement of thermoelectric properties of $MoS_2$. The devices has a heater line (black) to generate temperature gradient across $MoS_2$. The red and blue lines in four point probe configuration are used as temperature and Seebeck voltage sensors. The inner gold electrodes are used to measure electrical resistance of $MoS_2$ without contact contribution . . . . . . . . 32
3.6 Instrumentation used to measure $\alpha$ using the AC measurement technique . . . . . . . . . . . . . . . . . . . . . . . . . 33
3.7 Sample $R_0$ vs $T$ calibration curves for the sensors in four point probe configuration. Dotted lines are guidelines. . . . . . 35
3.8 $3\omega$ components measured in the sensor lines at room temperature as a function of squared of the applied heating voltage. Dotted lines are guidelines . . . . . . . . . . . . . . . 36
3.9 $\alpha$ vs $T$ measured using the $3\omega$ AC technique . . . . . . . . . . 36
3.10 Instrumentation used to measure $\beta$ using the AC measurement technique . . . . . . . . . . . . . . . . . . . . . . . . . 37
3.11 Lock-in amplifier reading of the amplitude of the Seebeck voltage as a function of the square of the sine-out heating voltage. A pre-amplifier gain of 10 is included in the y-axis readings. Dotted lines are guidelines . . . . . . . . . . . . . . . 38
3.12 Instrumentation used to measure $\alpha$ using the DC measurement technique . . . . . . . . . . . . . . . . . . . . . . . . . 40

3.13 A sample plot showing the quadratic dependence of the votlages in sensor line as a function of heating voltage. The quadratic coefficient is used to obtain $\alpha$. . . . . . . . . . . 41
3.14 Measured $\alpha$ as a function of temperature using DC technique . 41
3.15 Instrumentation used to measure $\beta$ using the DC measurement technique . . . . . . . . . . . . . . . . . . . . . . . . . . 42
3.16 Seebeck voltage measured using a DC voltmeter plotted as a function of the heating voltage. The departure from a perfect parabola is the result of the contributions to the Seebeck signal from the gate and the heater line. . . . . . . . . 43
3.17 Instrumentation setup used to measure the electrical conductance of $MoS_2$. . . . . . . . . . . . . . . . . . . . . . . . . 44
3.18 Seebeck coefficient of monolayer $MoS_2$ plotted as a function of temperature at various gate voltages. The solid lines are the fits obtained by using the Seebeck coefficient expression for transport by electrons activated to the mobility edge . . . 47
3.19 The plot of activation energy as a function of gate voltage. The activation energy slowly increases with increasing temperature. . . . . . . . . . . . . . . . . . . . . . . . . . . . . 47
3.20 Electrical conductance as a function of temperature on an Arrhenius plot. The electrical conductivity shows activated behavior at all gate voltages . . . . . . . . . . . . . . . . . . . 48
3.21 Seebeck coefficient of monolayer $MoS_2$ plotted as a function of temperature at various gate voltages. The solid lines are the fits obtained by using the Seebeck coefficient expression for transport by electrons activated to the mobility edge . . . 49
3.22 Summary of theoretical expressions for electrical conductivity and the Seebeck coefficient when localized and extended states are considered in isolation . . . . . . . . . . . . 50
3.23 The activation energy or energy gap obtained from the Seebeck coefficient fitting and from the electrical conductance data . . . . . . . . . . . . . . . . . . . . . . . . . . . . . . . 52
3.24 Peltier coefficient of monolayer $MoS_2$ plotted as a function of temperature at various gate voltages. . . . . . . . . . . . . . 53
3.25 The position of Fermi level from the mobility edge calculated from the Peltier coefficient measurements. The values are positive when the Fermi-level is under the edge. . . . . . . 54
3.26 Power factor $S^2\sigma$ of monolayer $MoS_2$ plotted as a function of temperature at various gate voltages. . . . . . . . . . . . . 55

4.1 Scanning electron microscopy image of the suspended bridge platform used to measure thermal conductivity of one-dimensional structures . . . . . . . . . . . . . . . . . . . . . . 58

4.2 Higher magnification SEM image of the heating and sensing membranes at the center of the device shown in Fig. 4.1. The sample to be measured is placed across the membranes . . . 59
4.3 Thermal circuit representing the heat flow pathways from the heating memebrane at temperature $T_H$ to the substrate at temperature $T_0$ . . . 60
4.4 Temperature rise on heating ($T_H - T_0$) and sensing ($T_S - T_0$) sides as the DC heating current is swept . . . 61
4.5 Images of the in-house biult transmission electron microscope holder that can accommodate the thermal conductivity measurement platform and align it to the electron beam inside a TEM . . . 64
4.6 Thermal conductance measured on a platform without any sample across the membranes. The measured conductance is the result of radiative and convective heat transfer between the membranes . . . 65
4.7 Thermal circuits representing the measurement scheme that accounts for asymmetry in thermal conductance of the beams on the heating and the sensing side . . . 66
4.8 Thermal conductance of the beams on the left and right side of the measurement platform. The difference is of the order of 1nW/K . . . 68

# CHAPTER 1

# INTRODUCTION

The focus of this dissertation is on the study of thermoelectric properties of one(1D)- and two-dimensional(2D) materials. More specifically, we study the Seebeck coefficient ($S$) and electrical conductivity ($\sigma$) of atomic layers of Molybdenum disulphide ($MoS_2$), a 2D material. For 1D materials, the focus is on the measurement technique to study phonon transport in ultra-low thermal conductance ($\kappa$) samples. The motivation behind these studies is two-fold. On one hand, we want to engineer and gauge these low dimensional materials for their applicability in practical thermoelectric devices. On the other hand, we want to advance the fundamental understanding of how a material's microstructure influences its thermal and electrical properties. This, in turn could enable deterministic engineering of the materials to make high performance thermoelectric devices. A brief background into the field of thermoelectrics is presented in the following paragraphs to help motivate the choice of materials in our study and to highlight the need to characterize the low thermal conductance 1D structures.

## 1.1 A brief background on thermoelectrics

Thermoelectric materials are primarily used for two applications: power generation or refrigeration as shown in Fig.1.1. In both the applications, the thermoelectric devices typically have a $\pi$ leg junction geometry which boosts their performance and allows easier integration with other electrical components [2]. In the power generating configuration, a thermoelectric material utilizes temperature gradient to generate electricity using the Seebeck effect. Conversely, in the heat pump/refrigeration configuration, electric current is passed through a thermoelectric material to achieve a temperature gradient by the Peltier effect. Both the configurations currently find use in a variety

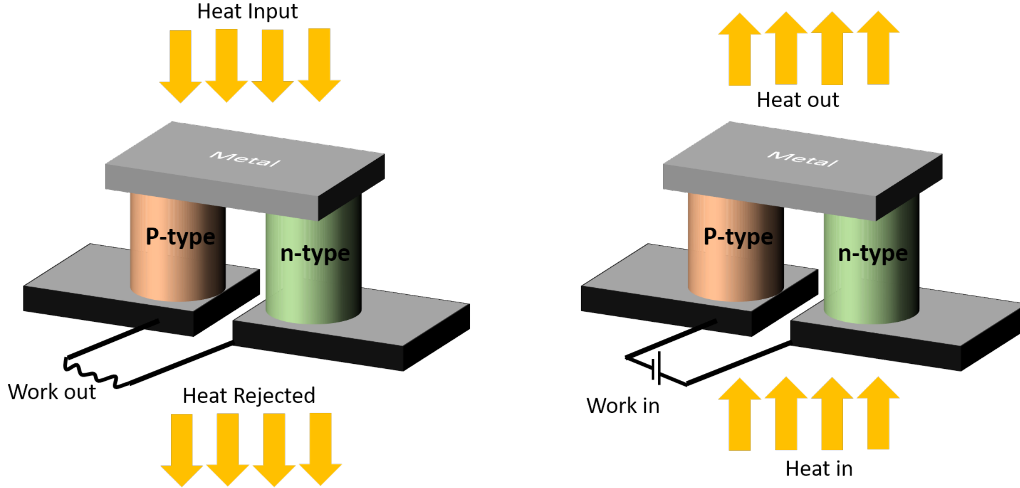


Figure 1.1: Schemtic of the thermoelectric devices for power generation(left) and for refrigeration(right).

of niche applications but their large scale deployment is hindered by their performance.

For example, the thermoelectric power generators are critical in small scale remote applications like deep space exploration. On a much larger scale, the thermoelectric power generators could utilize the waste heat from applications like automobiles, industrial plants and data centers to generate power. In 2016, out of 97 Quads of energy produced, nearly 66 Quads was rejected to the environment [3]. Assuming the average temperature of the heat rejected to be 150 C, a third of the rejected heat (22 Quad) could be harvested by a theoretical Carnot engine. However, the efficiency of the thermoelectric power generators is far below that of the efficiency of a Carnot engine, thereby hindering the applicability of the thermoelectric materials for power generation. If the efficiency of a thermoelectric device is even half as that of the Carnot efficiency, over 10 Quads of energy can be potentially harvested. A crucial metric called the thermoelectric figure of merit $zT = S^2\sigma T/\kappa$ determines the efficiency of the thermoelectric power generators as follows [4]:

$$\eta = \left(1 - \frac{T_C}{T_H}\right)\left(\frac{\sqrt{1+zT}-1}{\sqrt{1+zT}+T_C/T_H}\right) \tag{1.1}$$

where $T_H$ and $T_C$ are the temperatures of the heat rejecting hot surface and the ambient heat sink respectively. Notice that the first factor represents

the Carnot efficiency and the second factor represents the efficiency of the thermoelectric power generator as a fraction of the Carnot efficiency.

In a similar fashion, the coefficient of performance (COP) can be defined for the thermoelectric refrigerators/heat pumps as:

$$\eta = \left(\frac{T_C}{T_H - T_C}\right)\left(\frac{\sqrt{1+zT} - T_H/T_C}{\sqrt{1+zT}+1}\right) \tag{1.2}$$

The thermoelectric refrigerators are currently in use in niche applications like localized air-conditioning in automobiles [5] and remote coolers. Just like in the case of power generators, if made more effective, thermoelectric coolers could find use at a much larger scale in applications like micro-processor cooling [6].

Notice from Eq.1.1 and 1.2 that the efficiency of a thermoelectric power generator and the COP of the heat pump increase with increasing $zT$ and approach the Carnot values in the limit of $zT \to \infty$. It can be seen from Eq.1.1 that to obtain half the efficiency of the Carnot engine operating between 500 C and room temperature, a high zT value of 3 is required. It is extremely challenging to achieve such high zT values. zT values close to 0.5 were achieved as early as 1950s in bulk $Bi_2Te_3$ [7]. Gradual progress was made by doping or alloying the materials in the following two decades, reaching zT values as high as 1. The interest in the field of thermoelectrics diminished in the following years due to stagnation of experimental zT values around 1 [8]. However, theoretical papers [9] [10] highlighting the possibility of achieving high zT values due to quantum confinement in one and two- dimensional structures revived the interest in the field of thermoelectrics. The thermoelectric figure of merit in low dimensional materials was predicted to increase because of increased density of electron states (DOS) due to quantum confinement near the Fermi level compared to their bulk counterparts. Furthermore, it was also predicted that the expected lowering of thermal conductivity due to scattering of phonons at the boundary could boost the figure of merit for low dimensional materials. Improved values of zT have also been experimentally demonstrated in many materials by preparing them as two dimensional thin films/super-lattices or as one dimensional nanowires [11].

## 1.2 Motivation

*Thermal conductivity measurement of one-dimensional materials*

In the experimental studies on low dimensional materials, it has been observed that the gains in the thermoelectric figure of merit were mainly due to the reduction in thermal conductivity than by improvement of the power factor. As a result, the thermoelectric research community placed a heavy emphasis on finding ways to further push down the thermal conductivity of low dimensional structures while preserving their power factors. The suspended bridge measurement platform discussed in detail in chapter 4 played a pivotal role in studying thermal conductivity of the 1D maerials. In this technique, the thermal conductivity of an individual 1D sample is measured as opposed to measurement on an assembly of 1D structures in other techniques like $3\omega$ or TDTR. As a result, apart from just obtaining the thermal conductivity value at a certain temperature, this method enables researchers to correlate the microstructure and phonon transport in 1D materials.

For example, in a previous study carried out in our group, we measured the thermal conductivity of roughened silicon nanowires [12] as a function of temperature as shown in Fig.1.2. To study the influence of roughness on the thermal conductivity, we obtained the roughness profiles of nanowires made using the same procedure as the measured nanowire. The roughness profiles were obtained by stitching a series of images taken along the length of the wire inside a transmission electron microscope (TEM) as shown in Fig. 1.3. Using multiple scattering theory on the obtained roughness profile and modified Callaway model on the measured data at low temperatures, we were able to show that the roughness correlation length plays an important role in phonon scattering.

It is clear that this measurement technique enabled a fundamental study on the influence of the nanowire's microstructure (roughness) on its phonon transport. However, the microstructure characterization and the thermal conductivity measurement were done on different wires leaving an uncertainty in the conclusion made. This sort of uncertainty could become crucial in studies on ultra-thin wires wherein a small change in microstructure could change the thermal conductivity drastically. It is therefore necessary to develop methods that allow microstructure characterization and measurement on the same 1D structure. Further uncertainties could arise in studies on

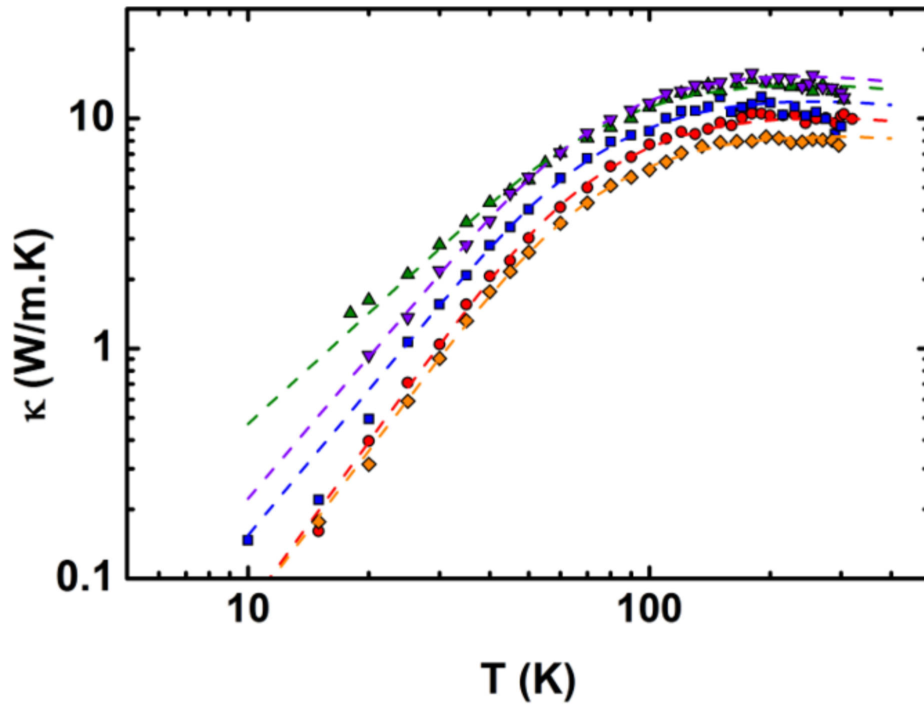


Figure 1.2: Thermal conductivity of nanowires measured as a function of temperature. Low temerpature data is used to obtain the boundary scattering rates for various roughness profiles

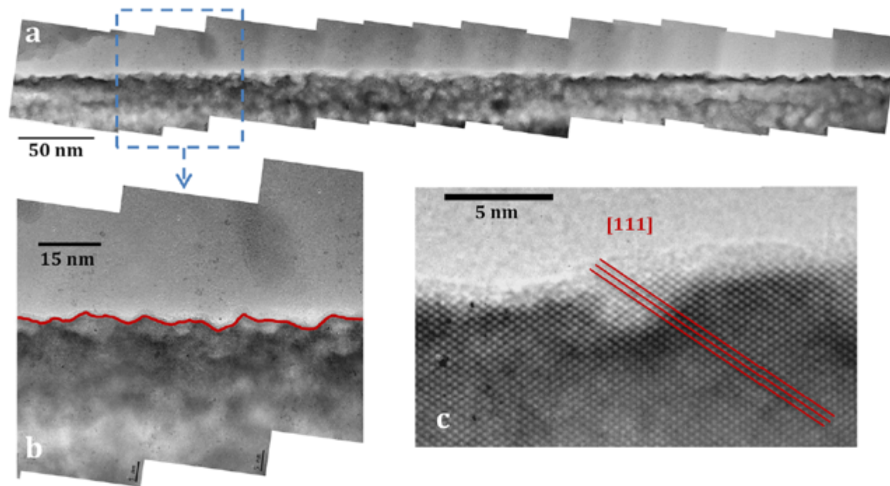


Figure 1.3: Roughness profile of silicon nanowires obtained by stitching a series of images taken in a transmission electron microscope.

ultra-thin wires that have a thermal conductances on the order of the conductance noise levels of the measurement. Various factors that contribute to errors in the thermal conductance have been identified and possible solutions have been proposed [13] [14] [15]. In chapter 4, we discuss the steps implemented in our lab to remove some of the systemic error sources and establish the lower limit of the thermal conductance measurement.

*Power factor measurement of two-dimensional materials*

As mentioned in the background section, semiconductor materials in their two-dimensional form have the potential to exhibit higher power factors ($S^2\sigma$) due sharp variations in their density of states as a result of quantum confinement. This has inspired the research into semiconductor materials in thin film and superlattice forms for thermoelectric applications over the past two decades and some gains have been demonstrated [16] [17] [18]. However, the promise of higher thermoelectric performance is yet to be tested comprehensively in the new class of semiconductor materials which crystallize as stacks of atomically thin two-dimensional layers. The atomic layers are held together in these materials by van der walls forces and can be isolated as fine as single atomic layers. $MoS_2$, a transition metal dichalcogenide, is perhaps the most studied material in this category. In its bulk form, it is usually used as a solid lubricant and has also been studied for its thermoelectric properties [19] and a power factor of around 35 $\mu W/m/K$ has been reported. This value is very small compared to around 10 $mW/m/K$ for commercially used $Bi_2Te_3$. However, when a single atomic layer of $MoS_2$ is isolated it shows remarkably different optical and electrical properties. This is because of the changing band structure as a function of number of layers isolated. The band gap is 1.2 eV and is indirect in its bulk form but the gap increases to 1.9 eV and becomes a direct band gap when $MoS_2$ is isolated as a single atomic layer [20] [21]. From electronics point of view, the wider band gap resulted in remarkable ON/OFF ratios and low standby power dissipation in the transistors made from monolayer $MoS_2$. The wider band gap is also favorable from the thermoelectric point of view. This is because, as a rule of thumb, the maximum achievable Seebeck coefficient increases with bandgap as $S_{max} = E_g/eT_{max}$ [22]. The maximum is achieved by moving the Fermi level away from the conduction band edge. However, moving the Fermi level away from the conduction band will reduce the conductivity due to reduced number of carrier concentrations. In view of these two behaviors,

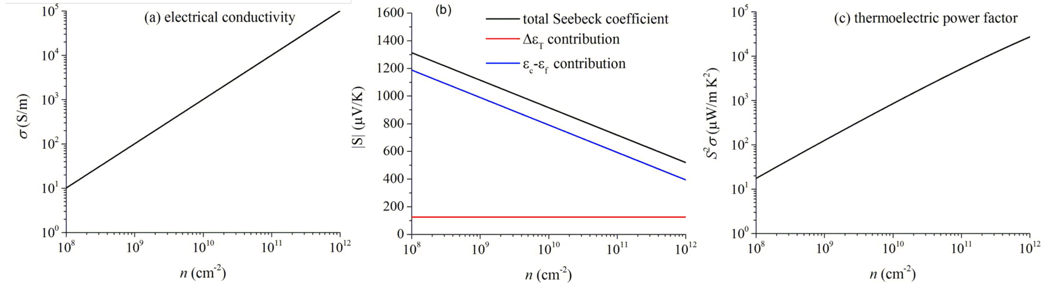


Figure 1.4: Semiclassical calculations of the thermoelectric properties of pristine $MoS_2$ with no localized states. Figure taken from ref [1]

it can be said there should exist an optimum Fermi level position where the power factor ($S^2\sigma$) is maximized.

Semi classical calculations based on Boltzmann transport equation [1] [23] done in our group for $MoS_2$. The study shows that the power factor actually increases monotonically as the Fermi level is moved closer to the conduction band by increasing the carrier concentration. This shows that the increase in conductivity is much stronger than the decrease in Seebeck coefficient. The Seebeck coefficient, electrical conductivity and the power factor obtained from this calculation are shown in Fig. 1.4.

Note that in the semi-classical calculations, $MoS_2$ was assumed to be pristine and suspended. A real $MoS_2$ sample will behave very differently due to presence of the localized states. The localized states are formed because of imperfections in the crystal. Sulphur vacancies in the crystal are the major source of these defects [24]. Adsorbed gas or water molecules, traps in the supporting substrate, oxidation of molybdenum are some of the other defects that create localized states. Temperature and carrier concentration dependence of the thermoelectric properties has been experimentally measured on mechanically exfoliated $MoS_2$ samples [25] [26] [27]. These studies show the presence of variable range hopping through the localized states [28].

The wide spread interest in the electrical and optoelectronic community has resulted in the development of a chemical vapor deposition (CVD) method [29] to grow $MoS_2$ in a laboratory setting. The localized states in the $MoS_2$ samples grown by the CVD process will depend on the growth process, and will differ from the mechanically exfoliated samples. Therefore, the thermoelectric properties are also expected to behave differently. Experiments have been performed to study the Seebeck coefficient and the electrical conductiv-

ity of CVD grown $MoS_2$ samples [30]. However, the measurement techniques used in the study can give erroneous results as a result of loading effects which are discussed in detail in chapter 3. Furthermore, the inferences drawn from these studies regarding the nature of the transport mechanism could be called into question.

From the above discussion, it can be clearly seen that there is a need to perform a thorough study of thermoelectric properties of these two-dimensional materials. Such a study will not only provide the magnitude of power factors in this material, but also provide fundamental insight into the transport mechanism. The current study on $MoS_2$ gains further importance as the models developed for one material could be used as a benchmark for hundreds of similar two-dimensional materials.

## 1.3 Thesis structure

The remaining chapters in this dissertation are structured as follows:

The focus of chapter 2 is on deriving the expressions for Seebeck coefficient and electrical conductivity when the electron transport takes place through the localized states. We begin by describing the differences between the extended and the localized states, in terms of their wave-functions and their transport mechanisms. Then, the problem of electrical transport through the localized states is reduced to that of a random network of resistors called the Miller Abraham's network. We then describe the percolation theory method that is typically used to analyze the Miller-Abraham's network. Assuming that $MoS_2$ has a step function like density of states, we apply the percolation theory method to obtain the expressions for the temperature dependence of the electrical conductivity and the Seebeck coefficient. Finally, a brief discussion on the temperature variation of Fermi level is provided.

Chapter 3 is focused on the experimental methods used to characterize the thermoelectric properties of $MoS_2$. We being by describing the steps that were followed to fabricate the devices that were used to measure the thermoelectric properties. Following that, we describe the AC and DC measurement techniques and corresponding instrumentation employed to measure the Seebeck coefficient. Advantages and disadvantages of both the techniques are described wherever relevant. Finally, the experimental results for the elec-

trical conductivity and the Seebeck coefficient are provided including their analysis.

In chapter 4, we focus on the measurement of thermal conductivity of one dimensional nanostructures. We begin the chapter with a description of the thermal conductivity measurement using the suspended bridge measurement platform. We then list the shortcomings of the measurement scheme and present the solutions that we have implemented to improve the measurement. In particular, we discuss an in house built transmission electron microscope holder that enables us to characterize and measure the same 1D structure.

Finally, in chapter 5, we present the possible future routes the research presented in this dissertation could take.

# CHAPTER 2

# THEORY OF THERMOELECTRIC PROPERTIES IN HOPPING REGIME

This chapter develops the theoretical framework within which we analyze and interpret our experimental results. In section 2.1, a distinction between extended and localized states is provided followed by a discussion on the their electron transport mechanisms. In section 2.2, the electrical conductivity ($\sigma$) and Seebeck coefficient ($S$) expressions for transport by the extended states is provided. The corresponding expressions for transport through the localized states are obtained by using the concept of Miller-Abrahams network and its simplification by percolation theory in section 2.3. The case of a step like density of localized states is considered in section 2.4 and the expressions for temperature dependence of electrical conductivity and Seebeck coefficient are derived. Finally, the derived expressions are further simplified by considering the statistical shift of Fermi level with temperature.

## 2.1 Extended and localized states

Consider a monolayer film of $MoS_2$ as shown schematically in Fig 2.1a. Under equilibrium conditions, the electrons represented by black dots in the figure are distributed uniformly throughout the film. If a non-equilibrium condition like an electric field or a temperature gradient is applied, the electron distribution will no longer remain uniform. When a temperature gradient is applied across the film as shown in Fig 2.1b, the electrons on the hotter side (left) will have more energy than the ones on the colder side. This results in more diffusion of electrons from left to right than in the other direction setting up an electron concentration gradient. By attaching an electrical load, as represented by a resistor in the figure, this buildup of charge can be tapped for useful work. Without any load attached, the electron concentration gradient completely manifests as a voltage difference across the film,

which is nothing but the Seebeck effect.

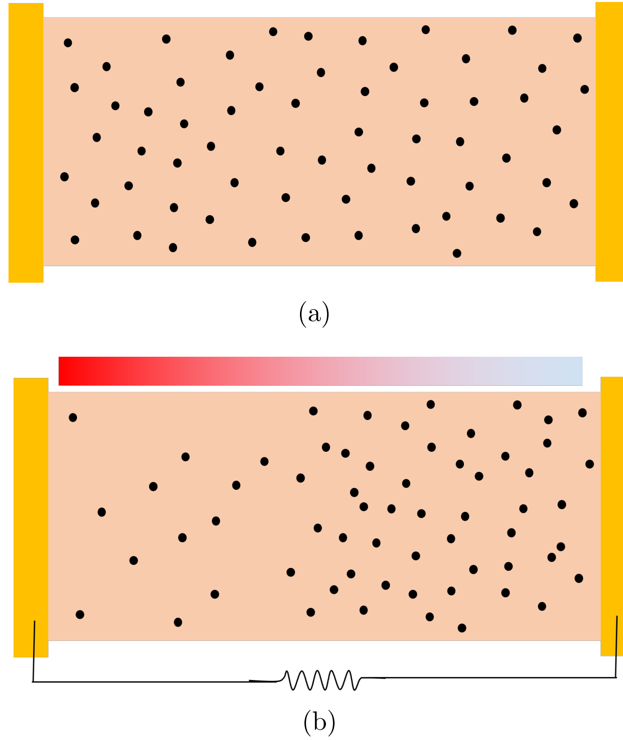

(a)

(b)

Figure 2.1: Schematic representation of electrons in an $MoS_2$ crystal in equilibrium and non-equilibrium conditions. Top: Electrons distributed uniformly throughout the crystal under equilibrium conditions. Bottom: Temperature gradient results in electron concentration gradient which can be used to run an electrical load

In the above description, the electrons have been described as if they were classical gas molecules. However, the electron are quantum particles, and per Paulis exclusion principle no two electrons can occupy the same electron state. The energies of the states available for electrons to occupy can be represented by dashes on a density of states schematic as shown in Fig 2.2. The states within the red boundary constitute the conduction band and the ones within the blue boundary form the valence band. The states right below the conduction band within the black boundary is called the conduction band tail. The terms $N_D$, $N_S$ and $\mu$ will be discussed in subsequent paragraphs.

The electron states within the tail differ from the ones in within the conduction or valence band in terms of their wave functions and transport mechanisms. The wave function of the conduction/valence band states span many inter-atomic distances, and in a perfect crystal they extend throughout the

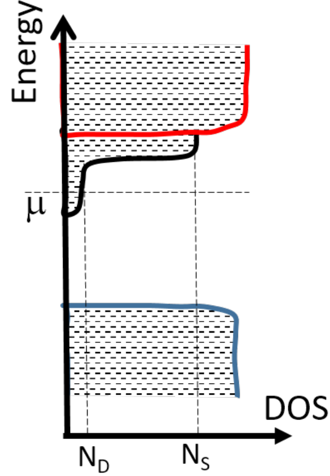


Figure 2.2: Schematic of density of states in $MoS_2$ crystal.The dashes represent the states the electrons can populate. Conduction and valence band states are bounded by red and blue lines respectively. The states bounded by the black line are the localized states that are formed because of imperfections in the crystal

entire crystal as shown schematically on the left in Fig 2.3. These states are therefore called the extended states. On the other hand, the wave function of a typical state in the conduction band tail is localized at a site and falls exponentially with the distance from the site as shown schematically on the right in Fig 2.3. An inverse localization length $\gamma$ can be defined such that the wave function of a localized states can be written as $exp(-\gamma R)$ The localization of electrons is caused by defects like vacancies, adsorbed molecules or reactions on the surface like oxidation etc. These defects trap the electrons close to their location resulting in localization of the states.

In terms of transport mechanism, the extended states accelerate under applied electric field till they undergo a scattering process with a phonon and lose their crystal momentum $(\hbar \overrightarrow{k})$. The transport of electrons in the localized states takes place by hopping process. In this process, a trapped electron absorbs or emits a phonon and hops to one of the sites that satisfy certain selection rules.

Note that crystal momentum cannot be defined for the localized states. The uncertainty $\Delta \overrightarrow{k}$ of these states is of the order of lattice constant, $a$. By Heisenberg's uncertainty principle, the uncertainty in its wave vector should

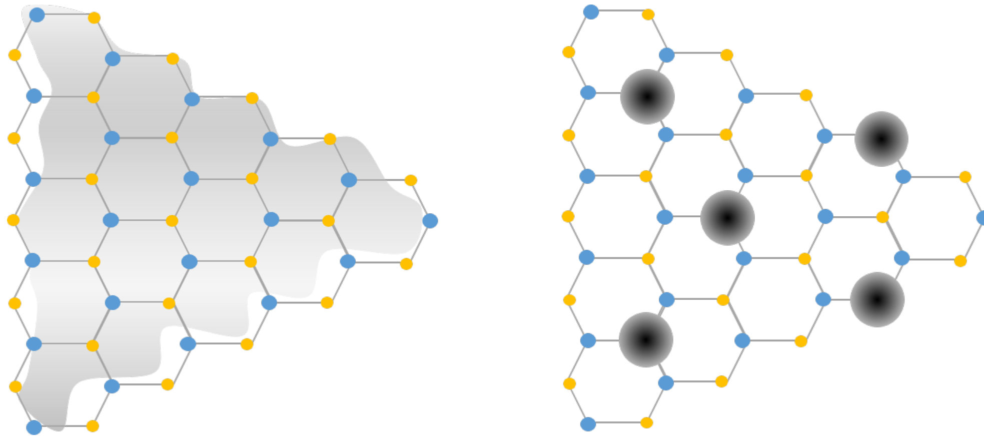

Figure 2.3: Schematic of the wavefunctions of extended (left)vs localized states (right). The wavefunctions of extended states span over the crystal and are not localized to one site. The localized sites on the other hand have wavefunctoins which die out within a few inter-atomic distances.

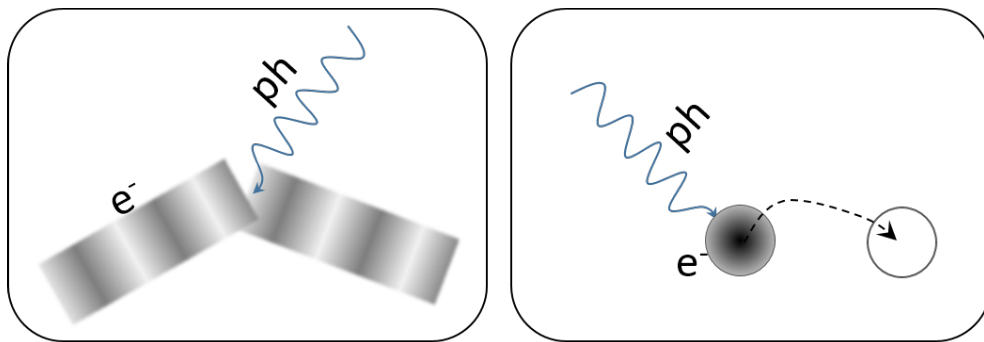


Figure 2.4: Schematic of the electron transport mechanisms of exteded states (left) and loclaized states (right).

be greater than $2\pi/a$ which is the entire width of the Brillouin zone. Thus, these states cannot be represented on a band diagram ($E$ vs $\overrightarrow{k}$) but only on a density of states plot.

As the temperature of the crystal increases, the population of phonon modes increases as per Bose Einstein distribution. This results in higher electron phonon scattering events thereby reducing the conductivity of electrons in extended states. However, for the localized states, the increase in phonon population assists the hopping process thereby increasing the conductivity.

As the number density ($n$) of electrons is increased in the solid, either by doping or by applying a gate voltage ($V_G$), the states in the tail are filled up first and followed by the states in the conduction band. Therefore, at low gate voltages where the localized states dominate the transport process, the electrical conductivity should show an increasing behavior with rising temperature. As the gate voltage is increased, the current is carried predominantly by the extended states and the conductivity should decrease with increasing temperature. This switch in temperature dependence of conductance as a function of carrier concentration is called the metal insulator transition.

## 2.2 Semi-classical model for $S$ and $\sigma$

The study of thermoelectric properties of disordered systems which have both localized and extended states was first carried out by Mott and coworkers [31]. In this approach, a differential conductivity function $\sigma(\varepsilon)$ is introduced such that current carried by electrons with energies between $\varepsilon$ and $\varepsilon + d\varepsilon$ under applied field $\mathbf{E}$ is given by $d\mathbf{j} = \sigma(\varepsilon)\mathbf{E}d\varepsilon$. Integrating this equation gives the total conductivity as $\int \sigma(\varepsilon)d\varepsilon$.

The expression for differential energy flux carried by electrons follows as:

$$(\varepsilon - \mu)\frac{d(j)}{e} = \frac{(\varepsilon - \mu)}{e}\sigma(\varepsilon)\mathbf{E}\, d\varepsilon \tag{2.1}$$

Integrating the equation gives the total heat flux carried by electrons, which is simply $\mathbf{j}\Pi$. Here, $\Pi$ is the Peltier coefficient which is related to the Seebeck coefficient as $\Pi = ST$. The expression for Seebeck coefficient can then be written as

$$S = -\int d\varepsilon \frac{(\varepsilon - \mu)}{eT} \frac{\sigma(\varepsilon)}{\sigma} d\varepsilon \tag{2.2}$$

From Eq.2.2, we can see that once the function $\sigma(\varepsilon)$ is known the thermoelectric properties can be determined. For transport by extended states, $\sigma(\varepsilon)$ can be defined using semi-classical approach under relaxation time approximation. Following Ref [32], the following expression can be written for the differential conductivity function for extended states in a 2D material.

$$\sigma_{ext}(\varepsilon) = e^2 N(\varepsilon) \int \frac{d^2\mathbf{k}}{2\pi^2} \delta(\varepsilon - \varepsilon(\mathbf{k})) \tau(\varepsilon) (\mathbf{v}(\mathbf{k}))^2 \left( \frac{-\partial f}{\partial \varepsilon} \right) \tag{2.3}$$

$N(\varepsilon)$ and $\tau(\varepsilon)$ are the denote the density of states and the relaxation time respectively of an electron at energy $\varepsilon$; $\mathbf{v}(\mathbf{k})$ is the group velocity of an electron with wave vector $\mathbf{k}$. Using Sommerfeld expansion, this expression leads to the popular Cutler Mott Equation for Seebeck coefficient

$$S = -\frac{\pi^2 {k_B}^2 T}{3e} \left[ \frac{d(ln(N(\varepsilon)))}{d\varepsilon} \right]_{\varepsilon=\mu} \tag{2.4}$$

This simple approach cannot be used reliably while considering conduction by hopping process for various reasons. Firstly, it is not possible to define $\mathbf{k}$ for localized states as discussed in the previous section. As a result, Eq.2.3 does not hold for these states. Secondly, an assumption implicit in the above analysis is that an electron with energy between $\varepsilon$ and $\varepsilon + d\varepsilon$ remains in that interval as it travels. Since hopping transport is essentially a series of inelastic electron-phonon scattering events, the assumption may break down.

Despite these limitations, the above analysis has been modified and applied by some authors [33] for transport by localized states. In such an analysis, the differential conductivity function is taken as

$$\sigma_{hop}(\varepsilon) = eN(\varepsilon)u(\varepsilon)k_B T \left( \frac{-\partial f}{\partial \varepsilon} \right) \tag{2.5}$$

$u(\varepsilon)$ is the mobility of the electrons with energy $\varepsilon$ and is defined by this equation. This approach gives the following modified expression of Seebeck coefficient.

$$S = -\frac{\pi^2 {k_B}^2 T}{3e} \left[ \frac{d(ln(Nu))}{d\varepsilon} \right]_{\varepsilon=\mu} \tag{2.6}$$

The derivation of this expression involves Taylor expansion of $(\varepsilon-\mu)N(\varepsilon)u(\varepsilon)$ about the Fermi level $\mu$. The Taylor expansion is valid only near the energies close to the Fermi level and provided that there are no steep changes to the function being expanded. Therefore, the above expression is invalid if there are steep changes to the density of states function close to the Fermi level. The validity of this expression is also suspect at intermediate to high temperatures where the states far away from the Fermi level contribute to the conduction.

Due to the above mentioned limitations, an alternative model which reduces hopping transport in a material to a random network of resistors is typically used. This random network of resistors called the Millers-Abrahams network is then solved for the thermoelectric properties using percolation theory methods as described in the following sections.

## 2.3 Miller Abrahams network and percolation theory

### 2.3.1 Miller Abrahams network

As mentioned in the previous section, an electron occupying a localized state travels by hopping to other localized sites by absorbing or emitting phonons. Consider two states localized at sites $i$ and $j$ separated by distance $R_{ij}$ with energies $\varepsilon_i$ and $\varepsilon_j$ respectively. The probability of an electron hopping from the state at $i$ to a state with higher energy at $j$ can be obtained using Fermi's Golden rule [34] as

$$W_{ij} = W_0 \, exp\bigg( -2\gamma R_{ij} - \frac{\varepsilon_j - \varepsilon_i}{k_B T} \bigg) \tag{2.7}$$

The factor $W_0$ depends on phonon deformation potential, phonon group velocity and overlap integral between the sites, and is a weak function of site energies compared to the accompanying exponential term.

Using 2.7, the electron transition rate $\Gamma_{ij}$ from site $i$ to $j$ can be written as $W_{ij} f_i (1 - f_j)$. Here, $f_i$ represents the occupation probability of site $i$ given by the Fermi-Dirac distribution. Under equilibrium conditions, the electron transition rate $\Gamma^0_{ij}$ can then be written and expanded (See Ch.10 in Ref [35]) as

$$\Gamma^0_{ij} = W^0_{ij}\, f^0_i\,(1-f^0_j) = A\,exp\bigg(-2\gamma R_{ij} - \frac{|\varepsilon_i-\mu|+|\varepsilon_j-\mu|+|\varepsilon_i-\varepsilon_j|}{k_BT}\bigg) \tag{2.8}$$

The equilibrium transition rate from $i$ to $j$ ($\Gamma^0_{ij}$) should be same as that from $j$ to $i$ ($\Gamma^0_{ji}$) due to detailed balance, resulting in a net zero transition rate between any two sites $i$ and $j$. However, when a non-equilibrium condition like an external electric field $\mathbf{E}$ is applied, the net transition rate between the sites ($\Gamma_{ij}$-$\Gamma_{ji}$) is no longer zero. In such a scenario, the occupation probability of any given site $i(f_i)$ deviates from its equilibrium value $f^0_i$ as a result of its non-zero transition rate interactions with all the other sites. It also changes with time if the applied field in time dependent. The rate equation which describes this time dependence can then be written as

$$\frac{df_i}{dt} = -\sum_j (W_{ij}f_i(1-f_j) - W_{ji}f_j(1-f_i)) \tag{2.9}$$

The applied field skews the electron scattering probability in the direction opposite to that of the applied field. This manifests as an additional term $-e\mathbf{E}.\mathbf{R}_{ij}/k_BT$ within the exponential in Eq. 2.7. So, the scattering probability term in Eq. 2.9 differs from its equilibrium value as $W_{ij} = W^0_{ij} + \delta W_{ij}$. Secondly, the occupation probability can be expressed as $f_i = f^0_i + \delta f_i$. This deviation appears because of the chemical potential $\mu$ in the Fermi-Dirac distribution. The applied field introduces spatial dependence of the chemical potential as opposed to a uniform value under equilibrium. With these considerations in mind, the rate equation can be linearized and written as

$$\frac{d\delta f_i}{dt} = -\sum_j \frac{\Gamma^0_{ij}}{k_BT}(U_i - U_j) \tag{2.10}$$

with $U_i - U_j$ being the generalized potential difference between sites $i$ and $j$ arising because of the applied electric field and the resultant spatially non-uniform chemical potential.

In physical terms, Eq.2.10 indicates that the rate of charge accumulation at a site $i$ is the sum of charge flow rates to all the other sites. This is analogous to Kirchoff's law for electrical circuits with current flowing between any two sites $i$ and $j$ being $(k_BT)^{-1}\Gamma^0_{ij}(U_i - U_j)$. This implies that a resistance can be defined between any two sites $i, j$ as $Z_{ij} = k_BT/\Gamma^0_{ij}$. Using Eq. 2.8, this

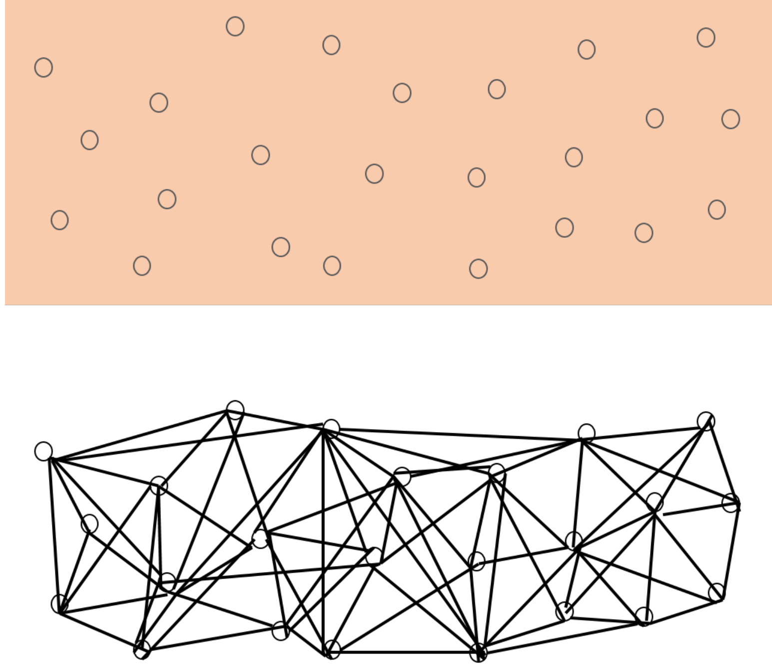

Figure 2.5: Miller Abrahams network formed by bonding each pair of hopping sites with a resistance decribed by Eq. 2.11

resistance can be written as

$$Z_{ij} = Z_0\, exp\left(2\gamma R_{ij} + \frac{|\varepsilon_i - \mu| + |\varepsilon_j - \mu| + |\varepsilon_i - \varepsilon_j|}{k_B T}\right) \tag{2.11}$$

Every pair of sites in the crystal can then be replaced by a bond of resistance defined by 2.11 as shown in Fig 2.5. This reduces the problem of finding the electrical conductivity of the crystal to finding out the overall resistance of the network [36]. Such a network is called the Miller-Abrahams network.

Given the vast number of bonds and their random resistance and spatial distribution, the Miller Abrahams network becomes difficult to solve in its entirety. To this end, percolation theory is very commonly used to identify a subset of the network called the critical network that can adequately describe the thermoelectric properties of the entire network.

### 2.3.2 Application of Percolation theory to Miller Abrahams network

We start by introducing a variable $\eta_{ij}$ which is defined as

$$\eta_{ij} = 2\gamma R_{ij} + \frac{|\varepsilon_i - \mu| + |\varepsilon_j - \mu| + |\varepsilon_i - \varepsilon_j|}{k_B T} \tag{2.12}$$

Clearly, $\eta_{ij}$ will vary depending on the energies and the separation distance of the sites. Assuming that this variation is uniform within a range $[-\eta_0\ \eta_0]$, the bonds in the network will have an exponential resistance distribution given by

$$Z = Z_0 exp(\eta) \tag{2.13}$$

To solve the Miller Abrahams network by percolation theory, all the bonds in the network are removed and then reintroduced into network in the ascending order of their resistance values. This process can be described mathematically by defining the so-called bonding criteria given by

$$2\gamma R_{ij} + \frac{|\varepsilon_i - \mu| + |\varepsilon_j - \mu| + |\varepsilon_i - \varepsilon_j|}{k_B T} < \eta \tag{2.14}$$

In this description, as $\eta$ is ramped up from $-\eta_0$ to $\eta_0$, the bonds which follow the bonding criteria are gradually reintroduced into the network. It is beneficial to define a metric representing the number of sites connected to a site of energy $\varepsilon_i$ at a given $\eta$ as

$$v(\varepsilon_i, \eta) = \int d\mathbf{R}_{ij} \int d\varepsilon_j N(\varepsilon_j) \theta \left( \eta - 2\gamma \mathbf{R}_{ij} - \frac{|\varepsilon_i - \mu| + |\varepsilon_j - \mu| + |\varepsilon_i - \varepsilon_j|}{2k_B T} \right) \tag{2.15}$$

where $\theta$ is the heavy side function to ensure that a bond is allowed only if the bonding criteria is obeyed.

We refer to this metric as the connectivity of a site and represent the connectivity averaged over all the sites of the network as $v(\eta)$.

As shown in Fig.2.6, as the $\eta$ value is increased and more bonds are added to the network, the reintroduced bonds coalesce and form chains of bonds called clusters. The average connectivity $v(\eta)$ also increases with increasing $\eta$ as shown in Fig 2.6 a,b. At a certain threshold value of $\eta = \eta_c$, a cluster spanning the entire crystal is formed as shown in Figure 2.6c. This cluster

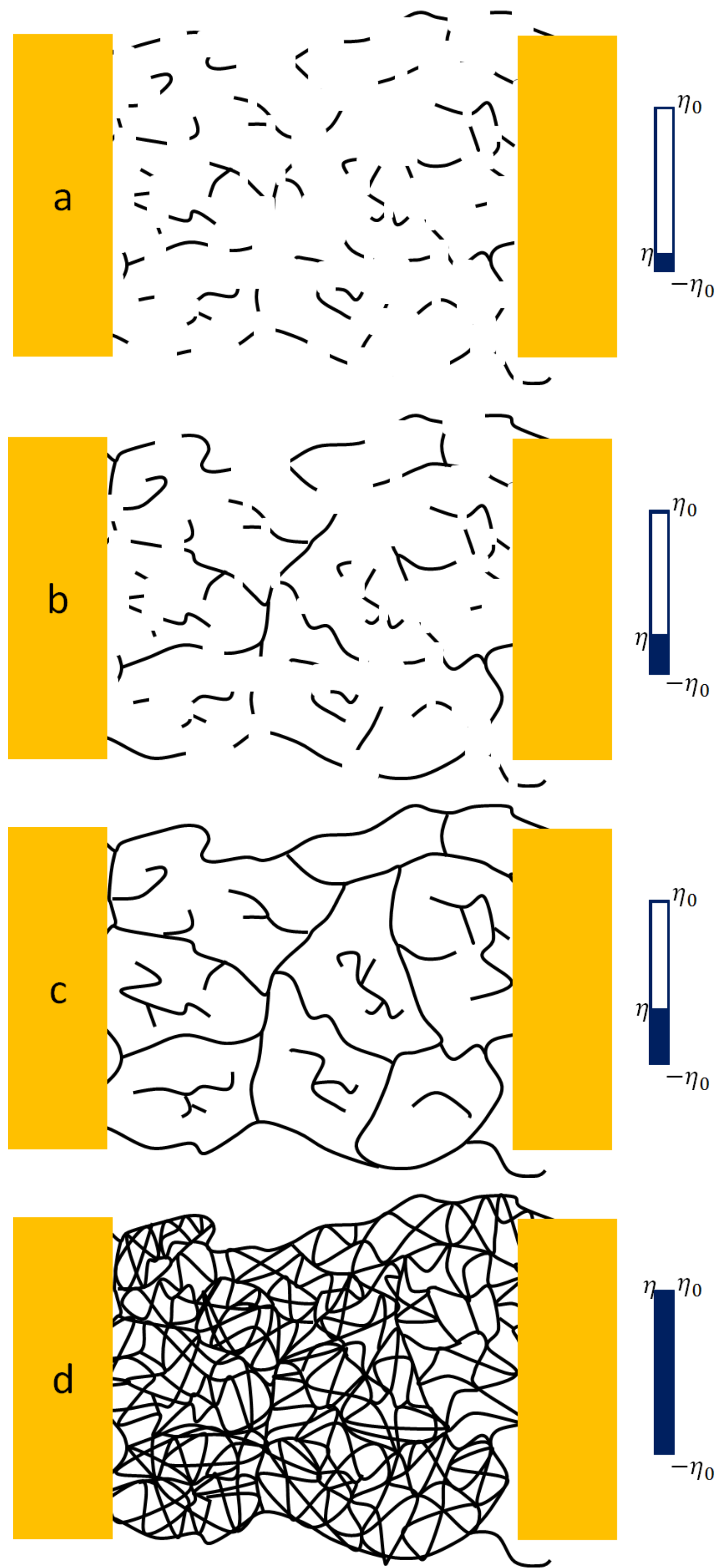


Figure 2.6: Schematic representation of the percolation theory method. All the bonds in the full network shown in (d) are removed and gradually reintroduced (a,b) till the percolation threshold (c) is reached.

is called the infinite cluster. Below $\eta = \eta_c$, the conductivity of the network is close to zero as there is no continuous pathway from one electrode to another. As $\eta$ value is further increased from $\eta_c$ to allow more bonds into the network, the conductivity of the network steeply increases from zero to a value close to the maximum possible conductivity of that of the entire Miller Abrahams network (Figure 2.6). Using numerical simulations, it has been shown that the real conductivity of the entire network is very close to that of the network formed at $\eta = \eta_c + 1$. The network at this juncture, composed of one infinite cluster and numerous finite clusters, is called the critical sub-network. Replacing the resistance of the bonds by the maximum resistance $Z_0 exp(\eta_c + 1)$ $Z_0 exp(\eta_c)$, the lower bound of the conductivity can be written as:

$$\sigma = \sigma_0 \, exp(-\eta_c) \tag{2.16}$$

The Seebeck coefficient of the entire network is obtained as that of the critical sub-network and is given by:

$$S = \frac{< \varepsilon - \mu >}{k_B T} = \frac{1}{k_B T} \frac{\int d\varepsilon (\varepsilon - \mu) \wp(\varepsilon)}{\int d\varepsilon \wp(\varepsilon)} \tag{2.17}$$

See Ch.5 in [37] for the derivation of this expression. Here, $< . >$ represents average over the sites in the critical sub-network and $\wp(\varepsilon)$ is the energy distribution function of the critical sub-network. $\wp(\varepsilon)$ can be written as the product of the density of states function $N(\varepsilon)$ and the probability $p(\varepsilon)$ that a site with energy $\varepsilon$ belongs to the critical sub-network. The probability is usually taken to be proportional to the connectivity $v(\varepsilon)$. This assumption makes intuitive sense because as the number of bonds converging on a site increases it becomes more likely to be included in the critical sub-network. In more rigorous terms, if $v(\varepsilon)$ is the average connectivity of a site, then the probability that it is connected to a specified number of sites is given by Poisson distribution. $p(\varepsilon)$ is approximated as the probability that a site is connected to two or more sites and is written as $p(\varepsilon) = 1 - (1 + v(\varepsilon)) exp(-v(\varepsilon)) \sim v(\varepsilon)$. Based on these arguments, the above given expression for Seebeck coefficient can be simplified as

$$S = \frac{1}{k_B T} \frac{\int d\varepsilon (\varepsilon - \mu) N(\varepsilon) v(\varepsilon)}{\int d\varepsilon N(\varepsilon) v(\varepsilon)} \tag{2.18}$$

## 2.4 Temperature dependence of thermoelectric properties

We apply the percolation method described above to a 2D material with step function density of states (DOS) as shown in Fig 2.2 with $N_D << N_S$ [38] [39]. The subscripts D and S stand for deep and shallow respectively. Note that in a real sample, the DOS function will be a more complicated function than a simple step function. The step functional form has been chosen as it results in simple expressions for the temperature dependence of electrical conductivity and Seebeck coefficient.

The condition $N_D << N_S$ implies that most of the localized states are shallow states which lie above the step location $\varepsilon_s$. In the model presented here, we assume that all the hopping interactions take place between the sites with energies greater than $\varepsilon_S$.

As described in the paragraphs above, we remove all the bonds and reintroduce them in the increasing order of their resistances. By substituting $|\varepsilon_i - \varepsilon_s|$ for $|\varepsilon_i - \varepsilon_s + \varepsilon_s - \mu|$ and simplifying, the bonding criteria given by Eq.2.14 can be written as:

$$2\gamma R_{ij} + \frac{|\varepsilon_i - \varepsilon_s| + |\varepsilon_j - \varepsilon_s| + |\varepsilon_i - \varepsilon_j|}{k_B T} < \eta - \frac{|\varepsilon_s - \mu|}{k_B T} \equiv \eta\prime \tag{2.19}$$

where $\eta\prime$ is defined by this equation. It is easy to note that the site energies $\varepsilon_i$ or $\varepsilon_j$ cannot exceed $\eta\prime k_B T$ for the bonding criteria to hold. So, the integrals in Eq. 2.18 and Eq.2.15 will be solved within the limits $[0 \quad \eta\prime k_B T]$

On further simplification, the bonding criterion can be written as

$$R_{ij} \leq \begin{cases} \frac{\eta\prime}{2\gamma} - \frac{\varepsilon_i - \varepsilon_s}{2\gamma\, k_B T}, & \text{if } \varepsilon_i > \varepsilon_j \\ \frac{\eta\prime}{2\gamma} - \frac{\varepsilon_j - \varepsilon_s}{2\gamma\, k_B T}, & \text{if } \varepsilon_j > \varepsilon_i \end{cases} \tag{2.20}$$

depending on whether energy is lost or gained respectively during the hop from site $i$ to site $j$.

Notice that in the first line of Eq. 2.20, the energy of the destination site $j$ does not appear. It implies that a site $i$ is allowed to bond with any site $j$ as long as its energy is lower ($\varepsilon_j < \varepsilon_i$) and it is within the radius $\eta\prime/2\gamma - (\varepsilon_i - \varepsilon_s)/2\gamma k_B T$. This can be represented geometrically as a cylinder of length $(\varepsilon_i - \varepsilon_s)$ and radius $\eta\prime/2\gamma - (\varepsilon_i - \varepsilon_s)/2\gamma k_B T$ on an energy-distance

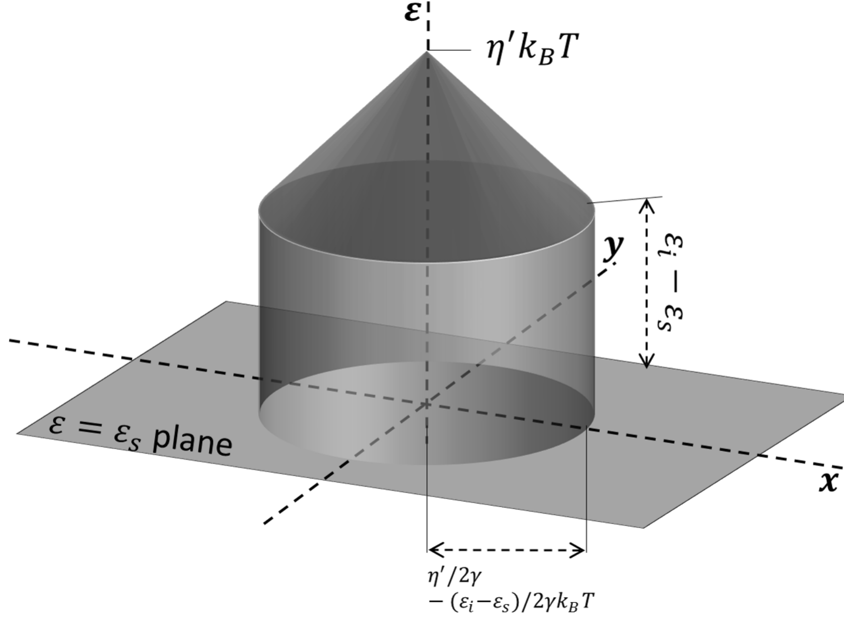


Figure 2.7: Geometry in a composit energy-distance space encompassing possible desitnation sites $j$ availbale to bond with site $i$ under bonding criteria given by Eq.2.20

composite space as shown in Fig.2.7 [40] [38].

Similarly, the bonds representing the hops from lower energy site to a higher energy site can be represented by a cone of height $k_B T\eta\prime - (\varepsilon_i - \varepsilon_s)$ and the same base radius as the cylinder.

For a constant density of states $N_S$, the connectivity of any site $i$ at a given $\eta\prime$ is then given by the product of density of states ($N_S$) and the volume of the object defined by the bonding criteria in Eq.2.20.

$$v(\varepsilon_i, \eta) = N_S \frac{\pi}{4\gamma^2}\left(\eta\prime - \frac{\varepsilon_i - \varepsilon_s}{k_B T}\right)^2 \left((\varepsilon_i - \varepsilon_s) + \frac{1}{3}(\eta\prime k_B T - (\varepsilon_i - \varepsilon_s)\right) \quad (2.21)$$

Note that for a more complex density of states function $N(\varepsilon)$, the connectivity will be given by the weighted sum of the density of states over the volume. The calculation in this case would be analogous to finding the mass of an object with non-uniform density.

Eq.2.21 can be simplified and averaged over all the sites $i$ such that $\varepsilon_i \in [0 \quad \eta\prime k_B T]$ to obtain the average connectivity $v(\eta)$. As discussed in the

previous section, the connectivity at the threshold condition $v(\eta_c)$ should be equal to $v_c$, which is obtained from numerical simulations.

$$v(\eta) = \frac{1}{24}\frac{N_S \pi k_B T}{4\gamma^2}\eta\prime^3 \tag{2.22}$$

Equation this expression to $v_c$ gives us the value of $\eta\prime$ and $\eta$ at threshold conditions

$$\eta_c\prime = \left(\frac{24 v_c \gamma^2}{N_S \pi k_B T}\right)^{1/3} = \left(\frac{T_s}{T}\right)^{1/3} \tag{2.23}$$

with $T_s = 24 v_c \gamma^2 / N_S \pi k_B$.
Strictly speaking, the averaging of Eq.2.21 over sites $i$ should be weighed by its occupation probability. This is because only the occupied sites will contribute to the conductivity. However, as noted in Ref. [38], this additional consideration will only change the numerical factor in $T_s$.
Using Eq.2.19 to find the $\eta_c$ from $\eta_c\prime$ and substituting it in Eq.2.16, the temperature dependence of conductivity is obtained as:

$$\sigma = \sigma_0 exp\left(-\frac{\varepsilon_s - \mu + k_B T (T_s/T)^{1/3}}{k_B T}\right) \tag{2.24}$$

From the above equation we can see that when the density of states function $N(\varepsilon)$ has a step function variation, Knowing $\eta_c$, Seebeck coefficient can be also calculated by using Eq.2.21 in Eq. 2.18as

$$S = \frac{k_B}{e}\left[\frac{\varepsilon_s - \mu}{k_B T} + \frac{3}{10}\left(\frac{T_s}{T}\right)^{1/3}\right] \tag{2.25}$$

Similar mathematical method can be applied for a more realistic density of states function like an exponential function: $N(\varepsilon) = N(\mu) exp(\frac{\varepsilon - \mu}{\varepsilon_t})$. Here $\varepsilon_t$ is the steepness of the exponential function [41] and $N(\mu)$ is the density of states at the Fermi-level position. This function becomes as step function when $\varepsilon_t$ approaches zero. For such a density of states function, the electrical conductivity can be written as $\sigma = \sigma_0 exp(-E_A/k_B T)$ with the activation energy $E_A$ given by:

$$E_A = \varepsilon_t exp(\frac{8\gamma^2 {k_B}^2 T^2 v_c}{\pi N(\mu) {\varepsilon_t}^3}) \tag{2.26}$$

The activation energy is a weak function of temperature. Therefore, the electrical conductivity should follow a straight line on an Arrhenius plot.

Finally, the Seebeck coefficient for the exponential density of states is given by $S = -(E_A - \varepsilon_t)/eT$.
In the expressions given above, the Fermi level $\mu$ is a function of temperature. So, the temperature dependence of the Seebeck coefficient depends on the dependence the behavior of Fermi level with changing temperature. This behavior of $\mu$ is called the statistical shift of the Fermi energy [42] and is discussed below.

### 2.4.1 Statistical shift of the Fermi energy

In a highly doped semiconductor or in a channel under high gate voltages, the thermally excited free carriers contribute very little to the overall carrier concentration near room temperature. The overall carrier concentration is fixed by the impurity concentration or the applied gate voltage. Consider the equation for number density of free carriers given by

$$n = 2\int d\varepsilon f(\varepsilon) N(\varepsilon) \tag{2.27}$$

where $f(\varepsilon)$ is the Fermi-Dirac distribution. If we now assume that the chemical potential is fixed and does not vary with temperature, then the number density has to change. If we assume a slowly varying density of states, we can apply Sommerfeld expansion to Eq.2.4.1. We the obtain the number density to be:

$$n = n_0 + \frac{\pi^2 k_B^2 T^2}{3} N'(\mu_0) \tag{2.28}$$

Here,$N\prime(\mu_0)$ is the derivative of the density of states function at the Fermi level position at absolute zero temperature, such that

$$N(\varepsilon) = N(\mu_0) + (E - \mu_0) N'(\mu_0) \tag{2.29}$$

The number density is however fixed by the doping concentration or by gating. Therefore, the Fermi-level should shift to compensate the increase in carrier density and keep it constant. If the Fermi level shifts by $\delta\mu$, roughly $2N(\mu_0)\delta\mu$ electrons can be reduced. Equating this term to the excess elec-

trons term in Eq.2.4.1, the shift in Fermi level can be written as

$$\delta\mu = \frac{\pi^2}{6}\frac{k_B^2 T^2}{} \frac{N'(\mu_0)}{N(\mu_0)} \tag{2.30}$$

Substituting the shift in Fermi level $\mu_0 - \delta\mu$ in Eq. 2.25, the temperature variation of Seebeck coefficient can be written as $S = A/T + BT + CT^{-1/3}$ with B representing the difference between the step location $\varepsilon_S$ and the Fermi level at absolute zero temperature $\mu_0$. A represents the quadratic coefficient of the rate at which the Fermi level drops as a function of temperature.

## 2.5 Conclusion

In conclusion, the theoretical framework required to analyze the measured thermoelectric properties has been developed in this chapter. The differences between the extended and the localized states in terms of their wave-functions and transport mechanisms are presented. The expressions for the Seebeck coefficient and the electrical conductivity for transport by extended states is reviewed. For transport by localized states, the material under consideration is reduced to a random network of resistors called the Miller-Abrahams network. The expressions for the Seebeck coefficient and the electrical conductivity are developed by solving this network using percolation theory for a step function density of states and exponentially varying density of states.

# CHAPTER 3

# EXPERIMENTAL INVESTIGATION OF THERMOELECTRIC PROPERTIES OF $MOS_2$ MONOLAYERS

## 3.1 Introduction

Over the past decade there has been an enormous interest in atomically thin two dimensional materials as they exhibit superior mechanical, electrical and thermal properties compared to their bulk counterparts. Graphene has received particular attention due to its easy preparation, high electrical and thermal conductivity, and mechanical strength. However, the lack of band gap in graphene limits its applicability in fields like electronics, optoelectronics, and thermoelectrics which require semiconducting materials. This requirement could be possibly met by a wide range [43] (nearly 600) of new two-dimensional materials which exhibit a variety of band gaps. Furthermore, hetero junctions can be made by selecting and stacking appropriate 2D materials to meet the requirements for any given application [44] [45]. Therefore, for the research community interested in thermoelectrics, a wide array of 2D materials and their hetero structures can be tested for their possible applicability. However, the study and interpretation of thermoelectric properties of these materials is not straight forward. Complications arise because of the presence of localized states which are formed by defects and exposure to ambient. While these complications are also present in bulk semiconductors, here they play a more deterministic role in the electron transport. It is therefore important to understand the role played by these localized states to be able to engineer the materials for thermoelectric applications.

Here, we study the thermoelectric properties of chemical vapor deposition (CVD) grown $MoS_2$ monolayers and specifically focus on the role of localized states in electron transport. We begin by describing the fabrication method used to prepare the sample for the measurement. We follow that with a description of the measurement technique and its limitations. Finally, we

present the data and interpret the data using the theoretical frame work provided in chapter 2.

## 3.2 Device fabrication and characterization

$MoS_2$ monolayers are grown [29] on a 285 nm silicon dioxide surface thermally grown on a heavily doped silicon substrate. The fabrication steps involved in the preparation of $MoS_2$ device for thermoelectric measurements are shown in Figure 3.1.

Using an optical microscope, we identify a clean and continuous $MoS_2$ film to be measured. Care is taken to make sure that the chosen film has no grain boundaries. Using e-beam lithography (PMMA 950A2-Microchem), we pattern $300\mu m$ x $300\mu m$ contact pads and lines leading up to the selected flake. A 5/200 nm Cr/Au film stack is used for pattering the pads and lead line. We use oxygen plasma to clean up the exposed areas before depositing the metal stack. The choice of the metal stack and the oxygen plasma step ensure easier ball-bonding process after the entire device is fabricated. Using a second e-beam lithography step, we cover the $MoS_2$ flake of interest with PMMA and etch away the neighboring $MoS_2$ flakes and any residue left over from the growth process. This ensures that the measurement is not contaminated by parallel flow paths though other $MoS_2$ flakes. Finally, the electrodes required for the measurement are patterned onto the $MoS_2$ flake and are connected to the lines leading to the contact pads. A stack of 5/10/200 nm of Ti/Pd/Au is deposited and the device is annealed at 420 K overnight to obtain achieve Ohmic contacts between $MoS_2$ and the metal electrodes as shown in Figure 3.2.

After the measurement on the sample is complete, we characterize the measured flake using Raman and photoluminescence (PL) to confirm that the sample measured in indeed a monolayer. The characterization is done after the measurement to prevent any possible damage to the flake due to laser irradiation. Fig 3.3 and Fig 3.4 show typical Raman and PL spectra observed for our samples. The peak difference of 19.28 $cm^{-1}$ in the Raman spectrum and the peak position at 1.85 eV in the PL spectrum indicate that $MoS_2$ grown is indeed in its monolayer form. We note that the PL spectrum shown in Fig 3.4 was taken on a random flake on the sample right after the

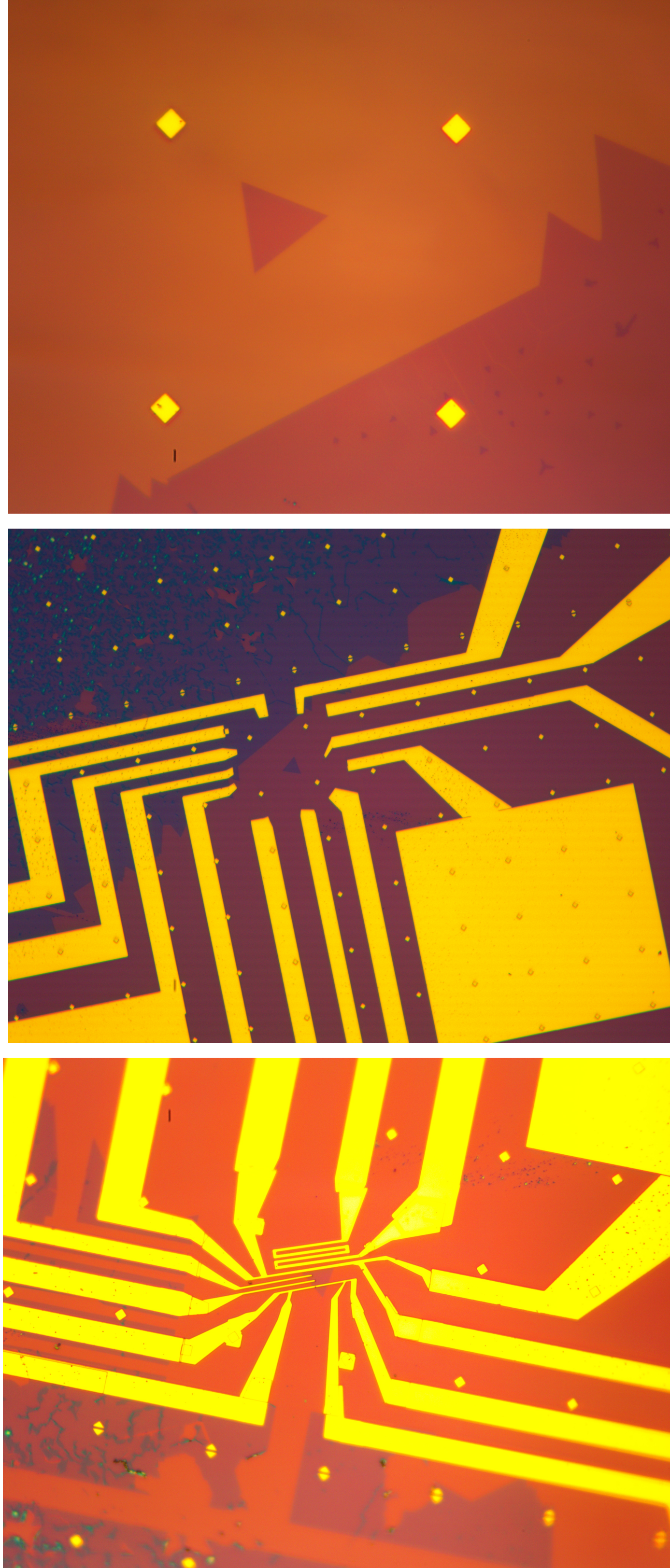

Figure 3.1: Images of the $MoS_2$ device at various steps of its fabricationn process

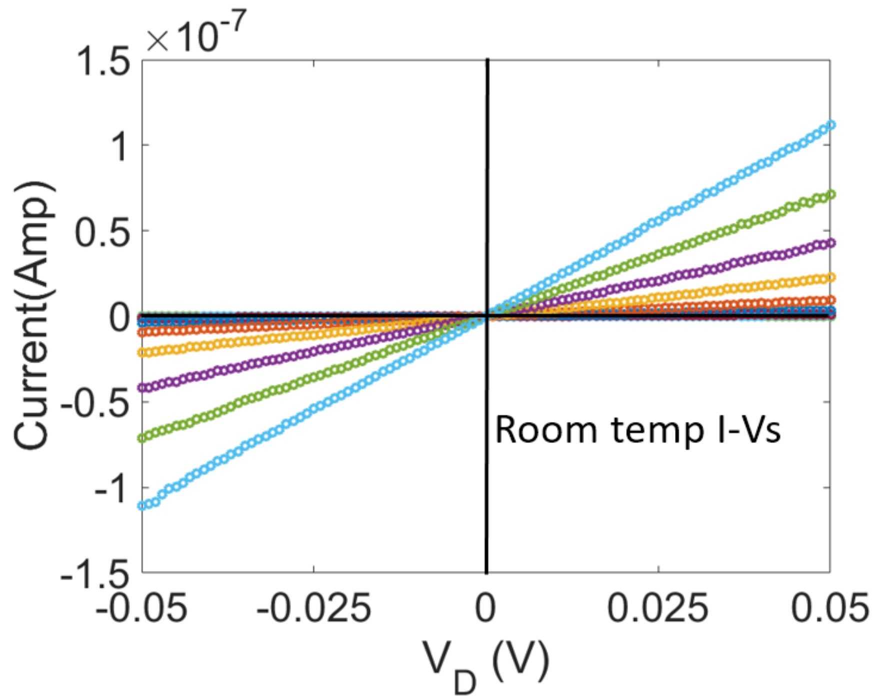


Figure 3.2: Linear $I$ vs $V_D$ curves at different gate voltages indicating Ohmic contacts between $MoS_2$ monolayer and Ti/Pd/Au metal stack

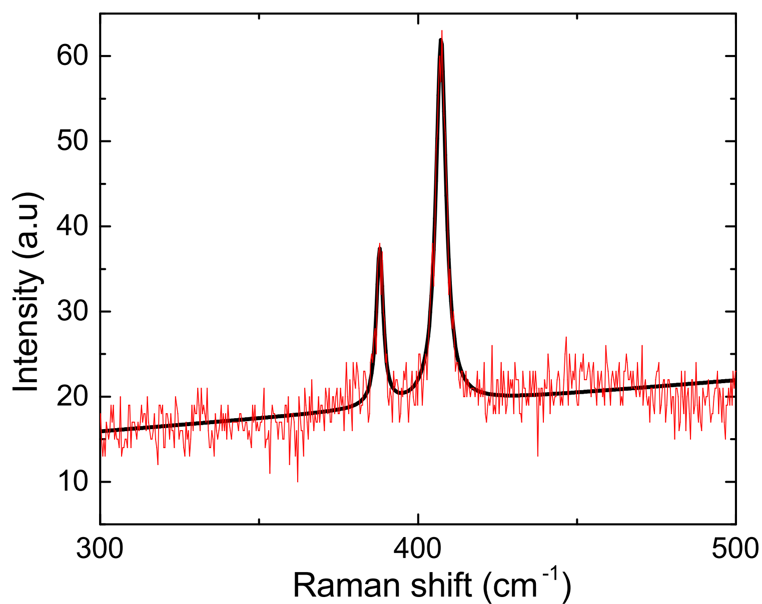


Figure 3.3: Typical Raman spectrum observed for the CVD grown $MoS_2$ monolayer used in this study. The black line represents the Lorentzian fit of the Raman shift data shown in red

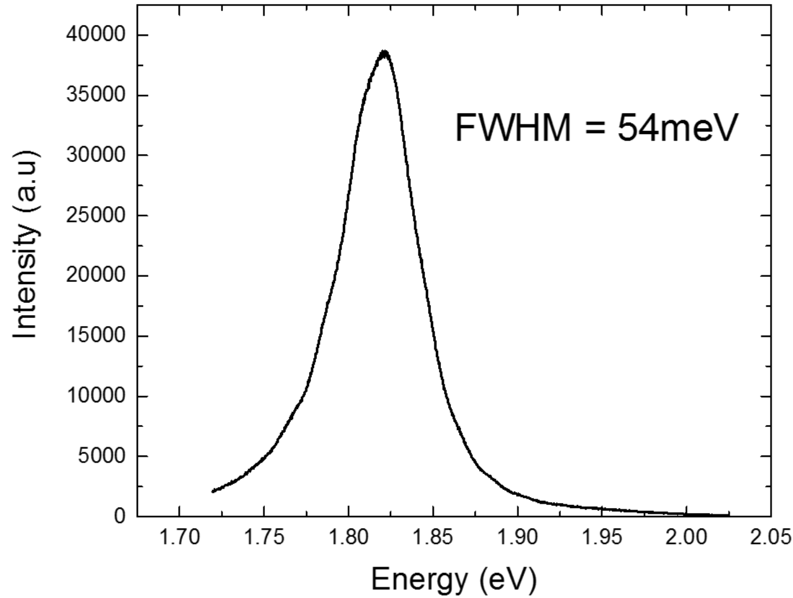


Figure 3.4: Photoluminescence spectrum observed for the CVD grown $MoS_2$ monolayer used in this study

growth process. We observed that the full width at half maximum (FWHM) of the actually measured samples is higher by around 30meV. The reason for the increase is currently not clear. Oxidation of $MoS_2$ or vacuum annealing after contact depositions could be the possible reasons.

## 3.3 Measurement principle and Instrumentation

### 3.3.1 Seebeck Coefficient

The measurement principal is easily understood with the help of the schematic shown in Fig.3.5. The device prepared for the measurement includes a heater line highlighted in black, two sensor lines in four point probe (4pp) configuration highlighted in red and blue, and two additional electrodes contacting $MoS_2$ channel between the 4pp sensor lines [46] [47]. The resistance of the heater line, and the red and blue sensor lines are denoted by $R_H$, $R_1$ and $R_2$ respectively. A heating voltage $V_H$ is applied across the heater line. The

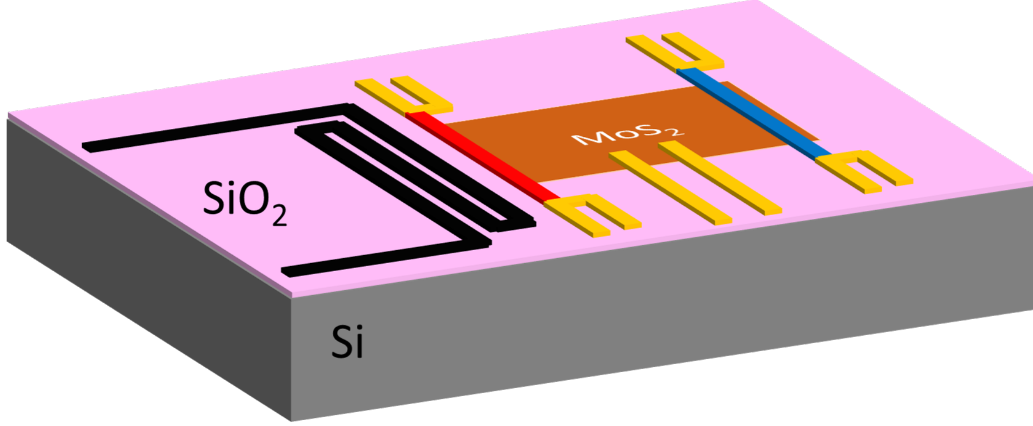


Figure 3.5: Schematic of the device fabricated for the measurement of thermoelectric properties of $MoS_2$. The devices has a heater line (black) to generate temperature gradient across $MoS_2$. The red and blue lines in four point probe configuration are used as temperature and Seebeck voltage sensors. The inner gold electrodes are used to measure electrical resistance of $MoS_2$ without contact contribution

Joule heat ${V_H}^2/R_H$ rises the temperatures of the red and blue sensor lines from bath temperature ($T_0$) to $T_1$ and $T_2$ respectively with $T_1 > T_2$. Due to the Seebeck effect, the temperature difference $T_1 - T_2$ creates a voltage difference of $V_{S1} - V_{S2}$ across the channel. The Seebeck coefficient is then obtained as the ratio of the voltage and the temperature differences or equivalently that of their gradients.

$$S = -\frac{V_{S1} - V_{S2}}{T_1 - T_2} = -\frac{dV_S/dx}{dT/dx} \tag{3.1}$$

with $x$ being the direction of the temperature gradient.

Note that the Seebeck voltage difference $V_{S1} - V_{S2}$ is an open circuit measurement. That implies that ideally no current should flow through the material under test during the measurement. Simultaneous measurement of the voltage and the temperature differences will result in the violation of the open circuit requirement. So, the measurement of Seebeck coefficient is split into two separate measurements by rewriting the expression for Seebeck coefficient as:

$$S = -\frac{d(V_{S2} - V_{S2})/d{V_H}^2}{d(T_1 - T_2)/d{V_H}^2} = -\frac{\beta}{\alpha} \tag{3.2}$$

By measuring the two proportionality constants $\alpha = d(T_1 - T_2)/d{V_H}^2$ and

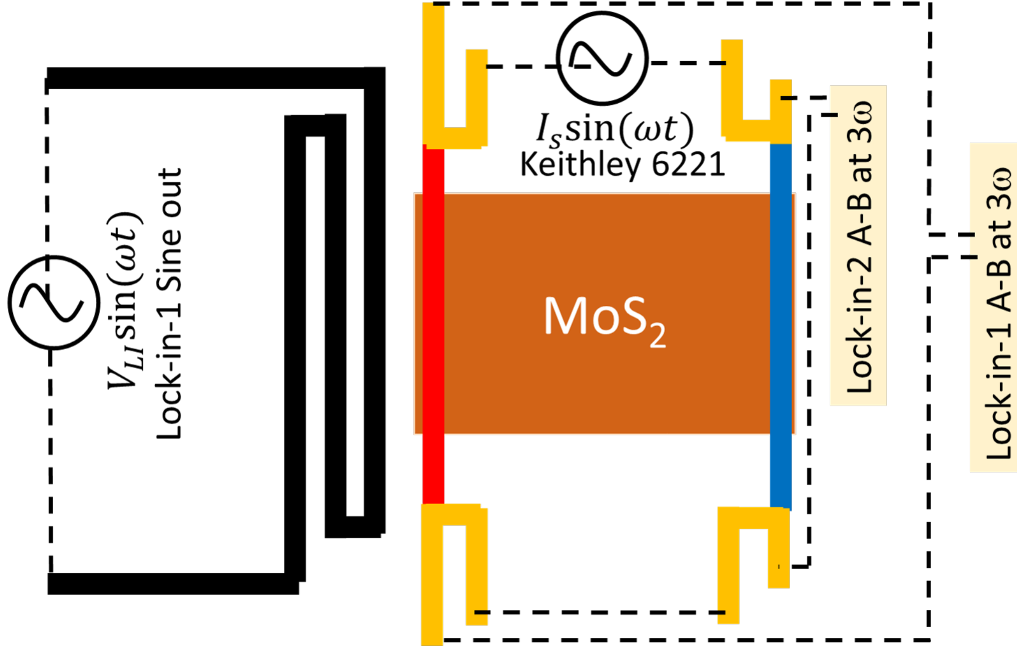


Figure 3.6: Instrumentation used to measure $\alpha$ using the AC measurement technique

$\beta = d(V_{S1} - V_{S2})/dV_H{}^2$ and taking their ratio, we can obtain the Seebeck coefficient. The measurement of these proportionality constants can be done using an AC technique wherein the applied heating voltage $V_H$ has a sinusoidal variation in time $V_H = V_H\, sin(\omega t)$. Alternatively, a DC technique with a steady DC voltage can be used. In the following sections, we discuss both the techniques and highlight their advantages and drawbacks.

#### 3.3.1.1 AC Measurement of $\alpha$

As mentioned in the previous section, a sinusoidal heating voltage $V_H\, sin(\omega t)$ is applied across the heater line in the AC technique. In our measurement technique, we use a lock-in amplifier's (SR-830) internal oscillator to apply the heating voltage as shown in Figure 3.6.

Keeping in mind that the lock-in reads and outputs root mean square (RMS) values, the applied heating voltage can be written as $\sqrt{2}V_{LI}\, sin(\omega t)$. Using the definition of $\alpha$, we can write the temperature difference across the $MoS_2$ channel as

$$T_1 - T_2 = 2\alpha V_{LI}{}^2\, sin^2(\omega t) = 2(\alpha_1 - \alpha_2)V_{LI}{}^2\, sin^2(\omega t) \tag{3.3}$$

$\alpha_1$ and $\alpha_2$ defined in the above equation are proportionality constants just like $\alpha$, but correspond to the temperature rises $T_1 - T_0$ and $T_1 - T_0$ respectively. By writing $2sin^2(\omega t)$ as $(1 - cos(2\omega t))$, we can see that the temperature rise of the sensor lines and their difference oscillates at twice the frequency $(2\omega)$ of applied gate voltage. As a result, the resistances of the sensor lines also oscillate at $2\omega$ as

$$R_{1,2} = (R_{1,2})_0 + \frac{d(R_{1,2})_0}{dT}(T_{1,2} - T_0) = (R_{1,2})_0 + \frac{d(R_{1,2})_0}{dT}\alpha_{1,2}{V_{LI}}^2(1 - cos(2\omega t)) \tag{3.4}$$

$d(R_{1,2})_0/dT$'s in the above equation are obtained as the slopes of the resistance vs temperature calibration curves taken at the measurement temperature $T_0$. The subscript 0 in $(R_{1,2})_0$ indicates resistance values measured at zero heating voltage. The calibration curves are obtained by measuring the resistances of the two sensor lines at various bath temperatures as shown in Figure 3.7. To obtain the slope at any required temperature $T_0$, we fit the $(R_{1,2})_0$ vs $T$ calibration curves using the Bloch-Gruneisen model. However, in the temperature range of our measurement (80 K and above), a linear fit provides $d(R_{1,2})_0/dT$ values close to the values from the Bloch-Gruneisen model.

Now, if a small sensing current $I_s\, sin(\omega t)$ at the same frequency as the heating current is passed through the two sensor lines, the voltage generated across the sensor lines has a $1\omega$ component and a $\omega$ component. The equation for this voltage is obtained by multiplying $I_s\, sin(\omega t)$ with $R_{1,2}$ from Eq. 3.4 followed by trigonometric manipulations

$$\begin{aligned} V_{1,2} &= R_{1,2} I_s sin(\omega t) \\ &= (sin(\omega t))\left((R_{1,2})_0 I_s + \frac{3}{2}\alpha_{1,2} I_s \,\frac{d(R_{1,2})_0}{dT}\, {V_{LI}}^2\right) \\ &+ (sin(3\omega t))\left(\frac{-1}{2}\alpha_{1,2} I_s \,\frac{d(R_{1,2})_0}{dT}\, {V_{LI}}^2\right) \\ &= (V_{1,2})_\omega \, sin(\omega t) + (V_{1,2})_{3\omega}\, sin(3\omega t) \end{aligned} \tag{3.5}$$

In our measurements, we use Keithley 6221 current source to pass $I_s = 4mA$ of peak current through both the sensor lines. Since the resistance of the $MoS_2$ channel is of the order of $M\Omega$s, the current leaking through

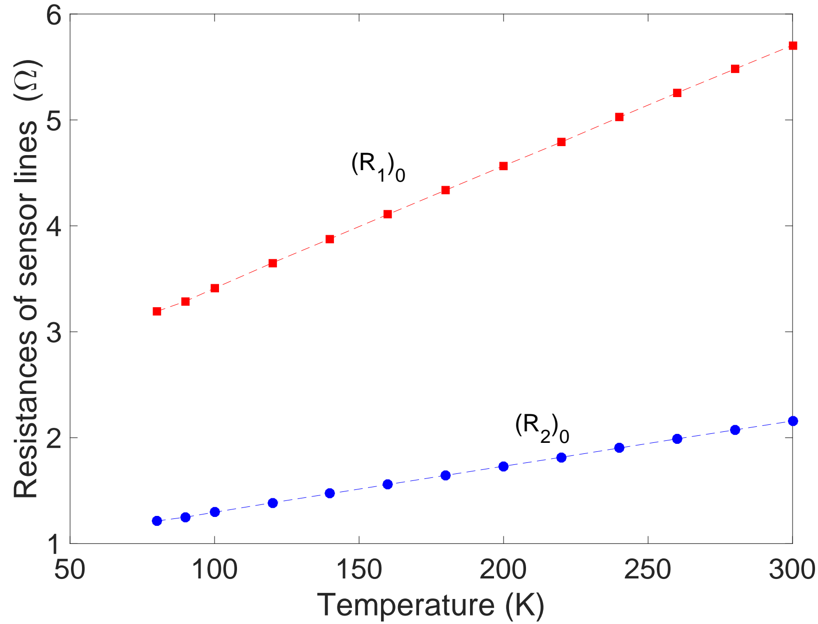

Figure 3.7: Sample $R_0$ vs $T$ calibration curves for the sensors in four point probe configuration. Dotted lines are guidelines.

the channel can be neglected. The choice of 4 mA is made to ensure that it is not high enough to disturb the temperature gradient created by the heating voltage while being high enough to generate a strong signal for our measurement.

Using two lock-in amplifiers synced to the Keithley 6221 current source and operating at third harmonic, we pick up only the $3\omega$ components across the sensor lines in Eq. 3.5. We the plot the measured $3\omega$ components as a function of the squared of the heating voltage supplied by one of the lock-ins ${V_{LI}}^2$ as shown in Figure 3.8. The straight lines are as expected from Eq.3.5. $\alpha_1$ and $\alpha_2$ can be obtained from the slopes of these lines as

$$\alpha_{1,2} = slope_{1,2} \cdot \frac{2\sqrt{2}}{I_s\, d(R_{1,2})_0/dT} \tag{3.6}$$

The additional factor of $\sqrt{2}$ appears because the lock-in amplifier measures RMS values while voltage terms in Eq.3.5 represent peak values. Finally, $\alpha$ is obtained as $\alpha_1 - \alpha_2$ by repeating this measurement at various temperatures as shown in Figure 3.9

*Note 1:* It is preferable to choose low heating frequency to ensure higher penetration depth $\sim \sqrt{1/\omega}$ [48] [49], which in turn results in higher temper-

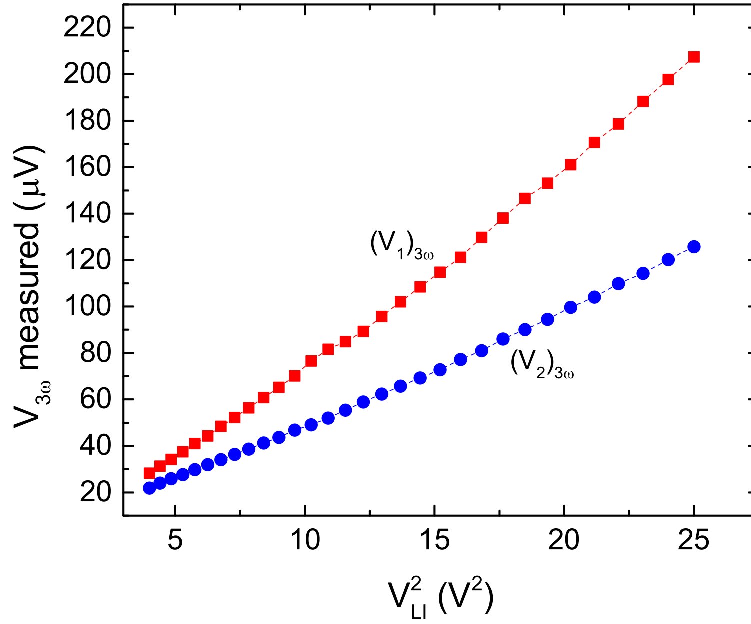


Figure 3.8: $3\omega$ components measured in the sensor lines at room temperature as a function of squared of the applied heating voltage. Dotted lines are guidelines

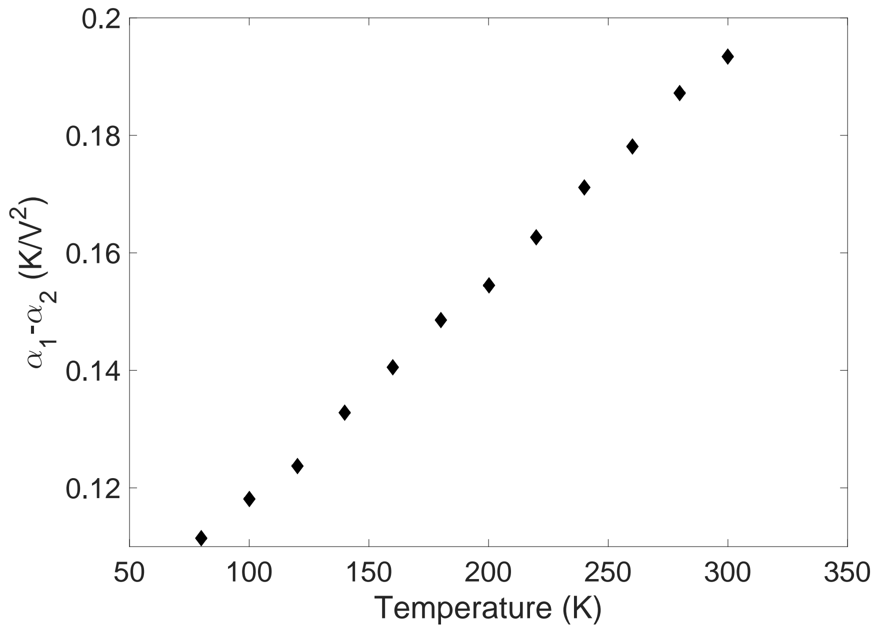


Figure 3.9: $\alpha$ vs $T$ measured using the $3\omega$ AC technique

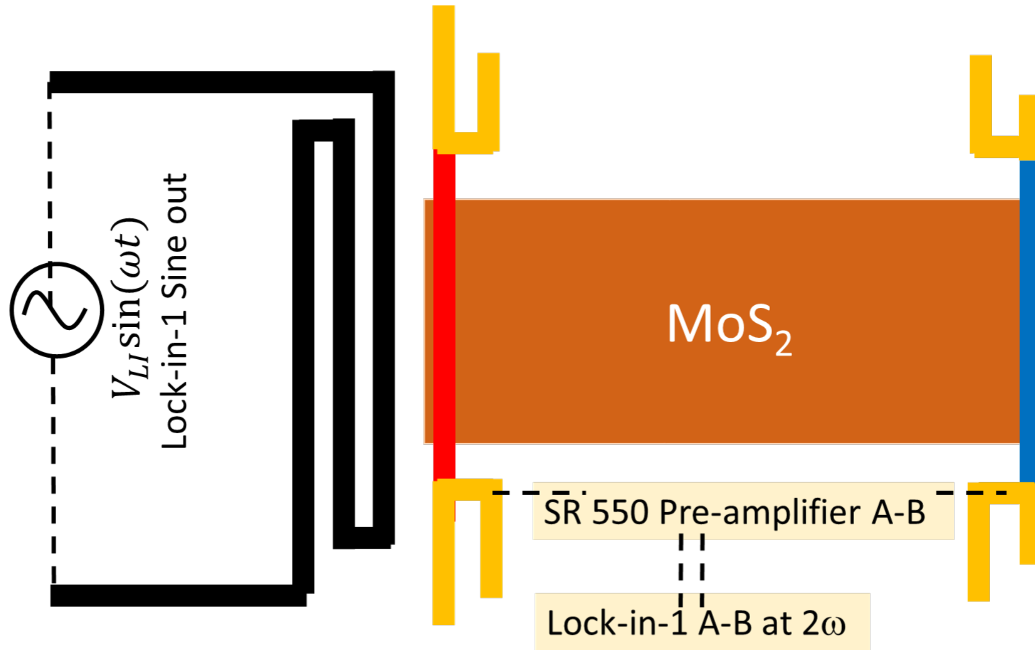


Figure 3.10: Instrumentation used to measure $\beta$ using the AC measurement technique

ature gradient. However, for very low frequencies, the time constant of the voltage measurement lock-ins need to be increased, which coul d slow down the measurement. We chose 4.3 Hz as the frequency and use 1-3 second time constant in the lock-in amplifiers.

*Note 2:* The applied voltage $V_L I$ does not appear fully across the heater line. This is because the heater line's resistance in our devices is comparable to the lock-in amplifier's output impedance of 50 $\Omega$. So, the alpha values measured could vary if an external oscillator with different output impedance is chosen. It is important to use the same source for measuring $\alpha$ and $\beta$.

#### 3.3.1.2 AC Measurement of $\beta$

The instrumentation used to measure $\beta$ using AC technique is shown in Figure 3.10. To measure $\beta$ at carrier concentrations, we use Keithley 2600 source meter to apply gate voltage to the silicon chip. As in the case of $\alpha$ measurement, the heating voltage is again supplied by the sine-out terminal of a lock-in amplifier and sets up a temperature difference across the $MoS_2$ channel.

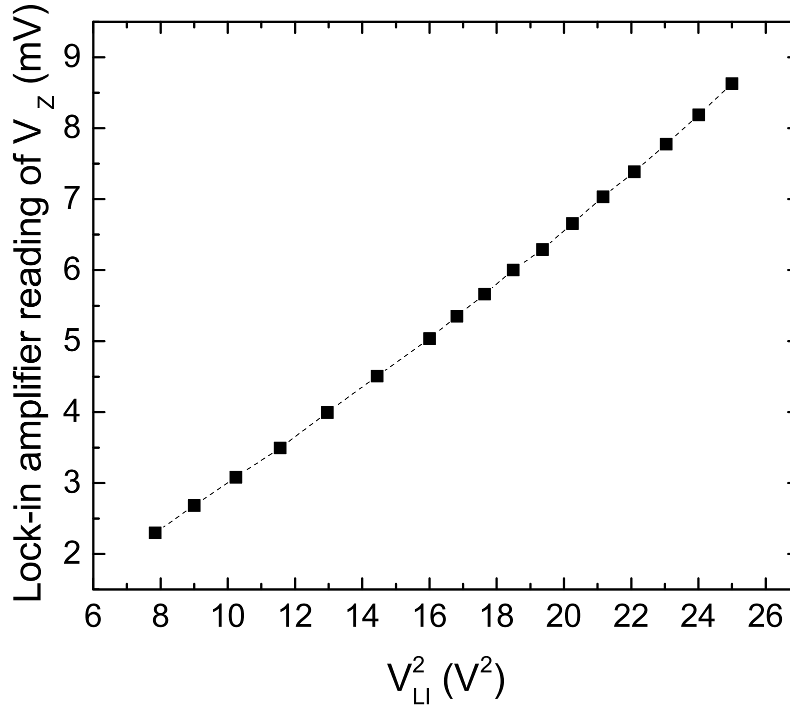


Figure 3.11: Lock-in amplifier reading of the amplitude of the Seebeck voltage as a function of the square of the sine-out heating voltage. A pre-amplifier gain of 10 is included in the y-axis readings. Dotted lines are guidelines

The Seebeck voltage difference developed across the channel can be written as:

$$V_Z = V_{S1} - V_{S2} = 2\beta {V_{LI}}^2 \, sin^2(\omega t) = \beta {V_{LI}}^2 \, (1 - cos(2\omega t)) \tag{3.7}$$

The factor 2 is to account for the fact that the sine out readings from a lock-in amplifier are RMS values. Notice that the Seebeck voltage oscillates at $2\omega$, twice the heating frequency $\omega$. Therefore, this voltage is read by using a lock-in amplifier under second harmonic settings. Furthermore, since $MoS_2$ is an n-type material, the voltage signal should be positive (more electrons on the cold side) giving a positive $\beta$ value. Rewriting $-\beta \, cos(2\omega t))$ as $\beta \, sin(2\omega t - 90))$, we see that the phase of the Seebeck voltage signal should be $-90^o$ out of phase with the internal reference signal for the lock-in ($sin(2\omega t)$). For a p-type material, the Seebeck voltage signal will have a phase shift of $+90^o$ and $\beta$ would turn out negative.

An additional instrumentation that becomes necessary in this measurement is a pre-amplifier. This is because the resistance of the $MoS_2$ channels used in our study are as high as $10 - 100M\Omega$ at low gate voltages. When a lock-in amplifier with an input impedance of $10M\Omega$ is directly used to measure the Seebeck voltages, the electrons will flow through the lock-in amplifier and the channel itself, violating the open-circuit measurement requirement. Therefore, the Seebeck voltages read directly by a lock-in amplifier are erroneous at low gate voltages where the channel resistances are very high. The use of an SR-550 pre-amplifier with an input impedance of $100M\Omega$ in our measurements allows us to measure Seebeck voltages at slightly lower gate voltages. Note that this pre-amplifier adds a constant gain of 10 to the measurement which needs to be accounted for during the analysis. If the control of the gain is desired, SR-560 pre-amplifier should be used.

The Seebeck voltage measured in this fashion is plotted as a function of the square of the heating voltage, ${V_{LI}}^2$ as shown in Figure 3.11. We obtain a straight line as expected from Eq. 3.7. The slope of this line can be used to obtain $\beta$ using the expression:

$$\beta = \frac{\sqrt{2}}{10} slope \tag{3.8}$$

Again, $\sqrt{2}$ is to convert the RMS values read from the lock-in amplifier to peak values.

The advantage of using the AC technique is that it prevents the contamination of the data due to leaks from the gate or from the heater line. This is achieved because of the use of lock-in amplifiers which effectively filter out DC leakage sources. While this technique is sufficient and preferable for low resistance channels, it gives erroneous results when materials with high resistances are being tested. Therefore, in order to study the thermoelectric properties of $MoS_2$ at low gate voltages where the localized states determine the transport properties, DC techniques are preferred. In the following two sections, we describe the DC techniques used to measure $\alpha$ and $\beta$.

#### 3.3.1.3 DC Measurement of $\alpha$

In the measurement of $\alpha$ by DC technique, a steady heating voltage $V_H$ is applied across the heater line using Keithley 2612 source meter as shown in

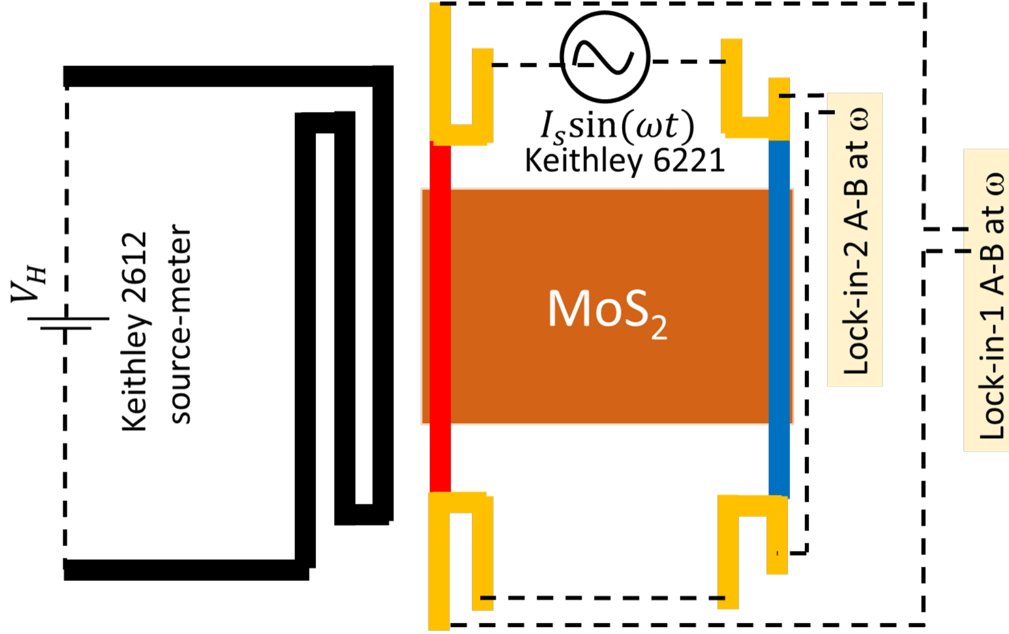


Figure 3.12: Instrumentation used to measure $\alpha$ using the DC measurement technique

Fig.3.12. This results in a steady temperature difference of $T_1 - T_2$ across $MoS_2$ which can be written as $\alpha {V_H}^2$. The resistances of the sensor lines also increase to a steady values given by:

$$R_{1,2} = (R_{1,2})_0 + \frac{(R_{1,2})_0}{dT}(T_1 - T_2) = (R_{1,2})_0 + \frac{(R_{1,2})_0}{dT}(\alpha_1 - \alpha_2){V_H}^2 \quad (3.9)$$

Now, if a sinusoidal sensing current at $I_s\, sin(\omega t)$ is passed through the sensor lines, the voltages in the sensor lines can be written as

$$V_{1,2} = R_{1,2} I_s\, sin(\omega t) = (R_{1,2})_0\, I_s\, sin(\omega T) + \frac{(R_{1,2})_0}{dT}(\alpha_1 - \alpha_2) I_s\, sin(\omega t)\, {V_H}^2 \quad (3.10)$$

The sensing current is passed through the sensor lines using Keithley 6221 current source and is kept low ($\sim 4mA$) to prevent excessive Joule heating. Two lock-in amplifiers synced to the current source are used to pick up the voltage signals at frequency $\omega$. The observed signals will have a quadratic dependence on the heating voltage $V_H$ as seen from Eq.3.10. By plotting the voltages measured as a function of applied voltage and taking the quadratic coefficients, the values of $\alpha_1$ and $\alpha_2$ can be obtained. A sample voltage vs

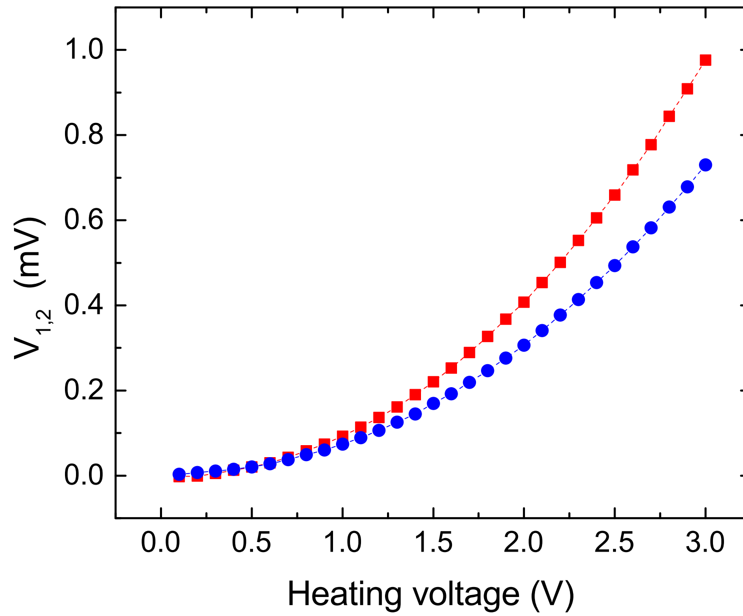


Figure 3.13: A sample plot showing the quadratic dependence of the votlages in sensor line as a function of heating voltage. The quadratic coefficient is used to obtain $\alpha$.

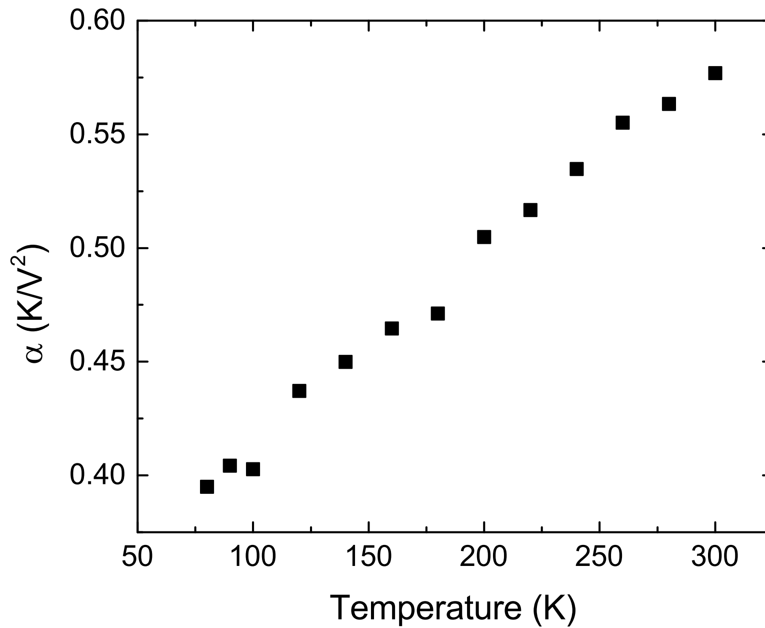


Figure 3.14: Measured $\alpha$ as a function of temperature using DC technique

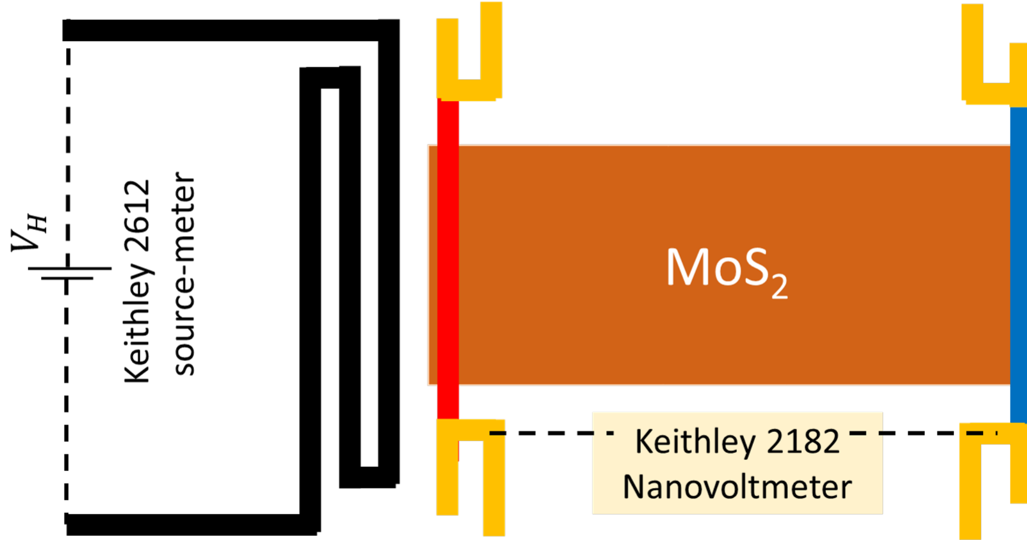


Figure 3.15: Instrumentation used to measure $\beta$ using the DC measurement technique

heating voltage plot is shown in Fig.3.14. We note that the curves in Fig.3.13 are offset by their minimum values to show the quadratic dependence more clearly. The values of $\alpha$ obtained by repeating this exercise at different temperatures is shown in Figure 3.14

We note that the sensing current is modulated at a frequency of 757 Hz in our experiments. This frequency is chosen as it is high enough for the lock-in amplifiers to filter out the DC leaks easily without having to resort to strong filters with high time constants.

#### 3.3.1.4 DC Measurement of $\beta$

The instrumentation for DC measurement of $\beta$ is shown schematically in Fig.3.15. Keithley 2612 source meter is used to apply the heating voltage $V_H$ to generate the temperature difference and corresponding Seebeck voltage. The Seebeck voltage has a quadratic dependence on the heating voltage and can be written simply as:

$$V_Z = \beta \, {V_H}^2 \tag{3.11}$$

The Seebeck voltage is then picked up using a Keithley 2182 nanovoltmeter. The nanovoltmeter connects to the measurement setup through a cable with

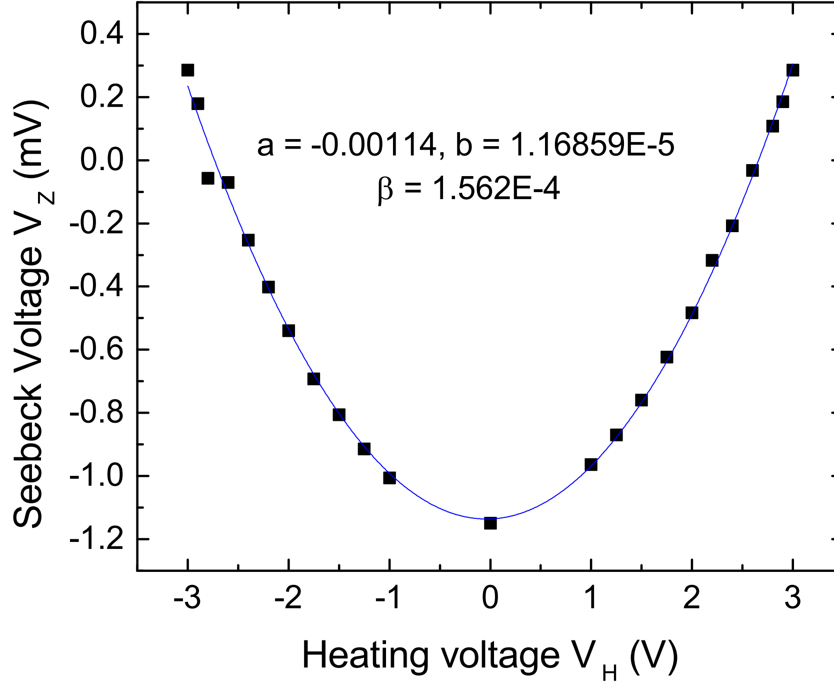


Figure 3.16: Seebeck voltage measured using a DC voltmeter plotted as a function of the heating voltage. The departure from a perfect parabola is the result of the contributions to the Seebeck signal from the gate and the heater line.

copper lug endings. The copper lugs easily oxidize and result in erroneous Seebeck voltage results. To prevent this, we replace the copper lug endings of the cable with BNC plugs using a silver solder.

Another challenge in using the DC method for Seebeck voltage measurement arises because of the leaks from the heater and the gate to the sensor lines. In the AC technique, the lock-in amplifier operating at $2\omega$ settings filter out the DC contribution to the signal from the gate and $1\omega$ contributions from the heater. However, the DC nanovoltmeter will not be able to distinguish the DC Seebeck signal from the heater and the gate contributions [26].

To overcome this problem, we sweep the heating voltage from negative to positive DC values and plot the measured Seebeck voltage as shown in Fig. 3.16. It is apparent from the figure that the curve does not completely follow the expression given in Eq.3.11. The curve could be represented more accurately as $V_Z = a + bV_H + \beta {V_H}^2$. In this expression, $a$ is the net result of

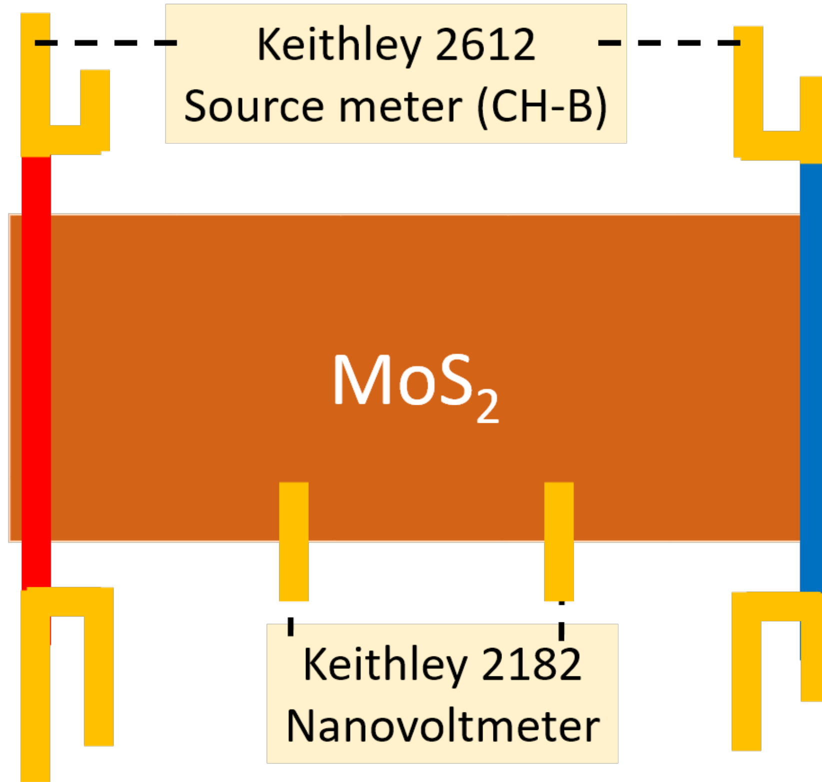


Figure 3.17: Instrumentation setup used to measure the electrical conductance of $MoS_2$.

the leaks form the gate and the residual voltage reading in the nanovoltmeter. This manifests as the non-zero reading at zero gate voltage in the $V_Z \, vs \, V_H$ plot. $b$ represents the signal contribution from the heater to sensor line leaks and manifests as the skewed nature of the parabola in the $V_Z \, vs \, V_H$ plot. By fitting a quadratic function and extracting the coefficient of ${V_H}^2$, we obtain the value of $\beta$.

Despite the challenges listed above, the DC method is the more reliable method for the study of Seebeck coefficient at low gate voltages. This is because of the high input impedance of the 2182 nanovoltmeter ($> 10G\Omega$) which is much greater than the channel resistance of $MoS_2$ at all positive gate voltages. This limits the current flow in the channel during the measurement, in near accordance with the open circuit requirement.

### 3.3.2 Electrical conductivity

Th measurement of electrical conductivity is done using the Keithley 2612 source meter the Keithley 2182 nanovoltmeter. Channel A of the source meter is used to apply the gate voltage while channel B is used to apply drain voltage across the two sensors lines as shown in Fig.3.17. Channel B also measures the resulting current. The nanovoltmeter is connected across the inner electrodes. The four point probe configuration removes the contribution of the contact resistance between the metal electrodes and the $MoS_2$ channel.

## 3.4 Results and Discussion

Figure 3.20 shows the temperature dependence of the measured electrical conductance (G) of an $MoS_2$ sample at various gate voltages. Notice that the plot is an Arrhenius type plot with log(G) plotted as a function of 1/T. We observe that at intermediate temperatures, the electrical conductivity displays an activated behavior at all gate voltages plotted. At higher temperatures, we observe a slight deviation with the conductance exceeding the activated behavior and then decreasing with temperature. At low temperatures, the conductance flattens out and deviates from the activated behavior. These observations could be explained by two possible hypothesis. The first hypothesis assumes that the activated behavior is due to the electrons jumping from the Fermi level to the mobility edge [50]. Under these conditions, the conductivity can be written as:

$$\sigma = ne\mu = e\mu(T)N_C exp(-\frac{\varepsilon_C - \varepsilon_F}{k_B T}) \tag{3.12}$$

Here $\varepsilon_C$, $\varepsilon_F$ and $\mu$ represent the conduction band ege, Fermi level, and the mobility respectively. $N_C$ is the density of states at the conduction band edge. Strictly, speaking, $\varepsilon_C$ is the location of the mobility edge above which demarcates the localized and the extended states. The overall conductance data can then be interpreted using this equation as follows: The exponential factor contributes to the activation region in log(G) vs 1/T curve. The deviation from the activation behavior at high temperatures is attributed to the change in mobility. At higher temperatures, the mobility increases due to impurity scattering which favors forward scattering [51] and then falls due

to electron-phonon scattering which is a randomizing scattering mechanism. At low temperatures, the conduction is carried out only by the electrons occupying the localized states in the vicinity of the Fermi level $\varepsilon_F$ and the conduction band states do not contribute to the current flow. Under such conditions, variable range hopping through the localized states is expected to dictate the conduction as $log(G) \sim T^{-1/3}$, therefore explaining the flattening in the log (G) vs 1/T curve. As the gate voltage is increased, the Fermi level moves closer to the conduction band edge and the variable range hopping mechanism fades out, thereby removing the flattening effect.

Note that the activation behavior persists till the maximum applied gate voltage of 60 V, which should correspond to high carrier concentrations. However, the carrier concentration at 60 V is not very high in our sample due to high threshold voltages as shown in Fig. 3.18. The threshold voltage ($V_H$) for this sample is between 20 V to 30 V depending on the temperature. Assuming a nominal value of 25 V for threshold voltage, 60 V back gating should give a carrier concentration of 2.58x$10^{12}/cm^2$. We obtained this number using a parallel plate formula for carrier concentration: $n = \frac{C_{ox}}{e}(V_G - V_{Th})$, where $C_{ox}$ is the capacitance of 285 nm of silicon dioxide taken as 1.18 x $10^{-4} Farad/m^2$.

Also note that the activation behavior is not perfect. In fact, the log(G) vs 1/T fit gives different activation energy values depending on the range of fitting. In Fig.3.19 two activation energy plots are plotted as a function of applied back gate voltage. The top curve is obtained by fitting the data between 200 to 260 K. The bottom curve is fit between 120 to 180 K. This indicates that the activation energy is increasing with increasing temperature. This could be attributed to the statistical shift of Fermi level with temperature as discussed in Chapter 2.

The second hypothesis attributes the activated behavior to the hopping mechanism through the localized states in the band gap. As per the mathematical framework provided in chapter 2, the activation energy in such a regime is given as: $E_A \sim \varepsilon_t ln(T^2/N(\varepsilon_F))$, where $\varepsilon_t$ is the steepness of the density of localized states and $N(\varepsilon_F)$ is the density of states at the Fermi-level position. The density of localized states in the band-gap has been reported to be an exponential function using capacitance measurements on CVD grown $MoS_2$ films [50]. As a result the activation energy takes the form $E_A \sim const - \varepsilon_F$. As the gate voltage increases, the Fermi-level moves

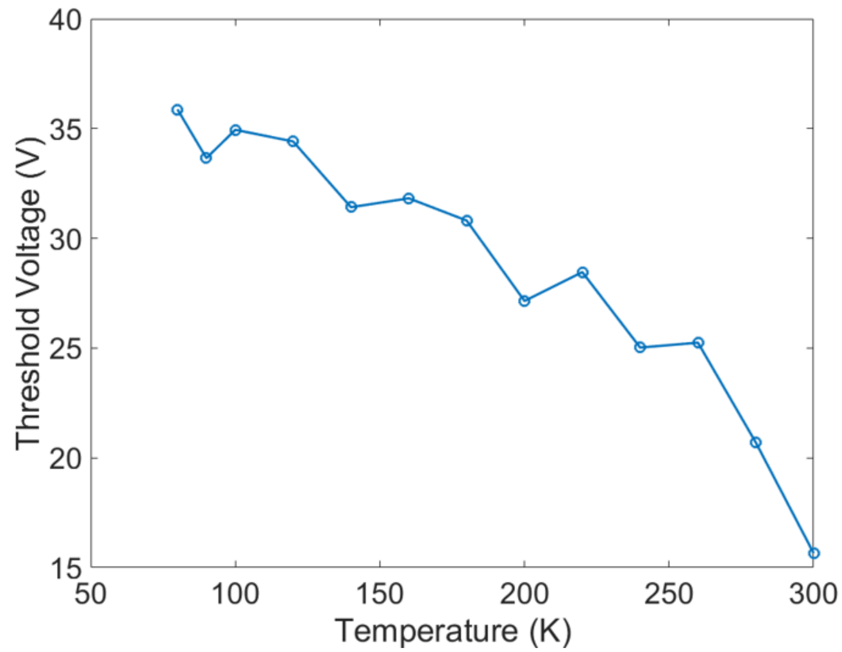


Figure 3.18: Seebeck coefficient of monolayer $MoS_2$ plotted as a function of temperature at various gate voltages. The solid lines are the fits obtained by using the Seebeck coefficient expression for transport by electrons activated to the mobility edge

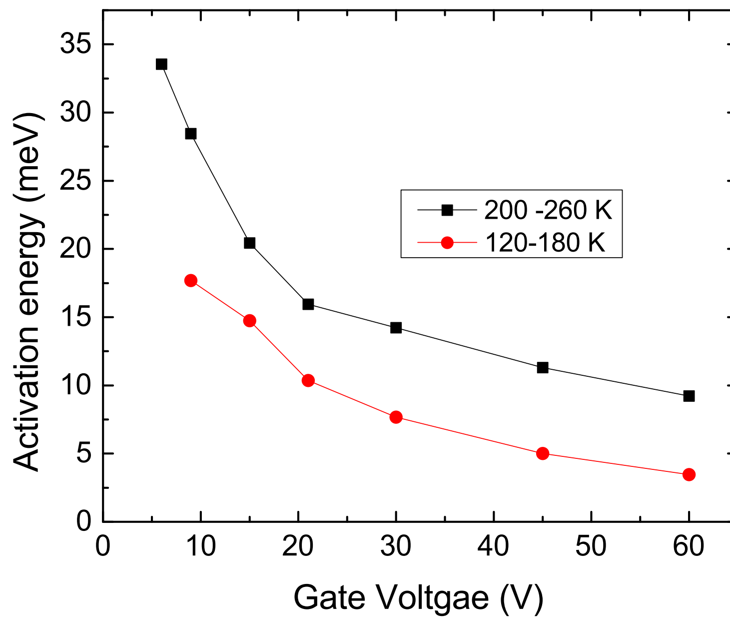


Figure 3.19: The plot of activation energy as a function of gate voltage. The activation energy slowly increases with increasing temperature.

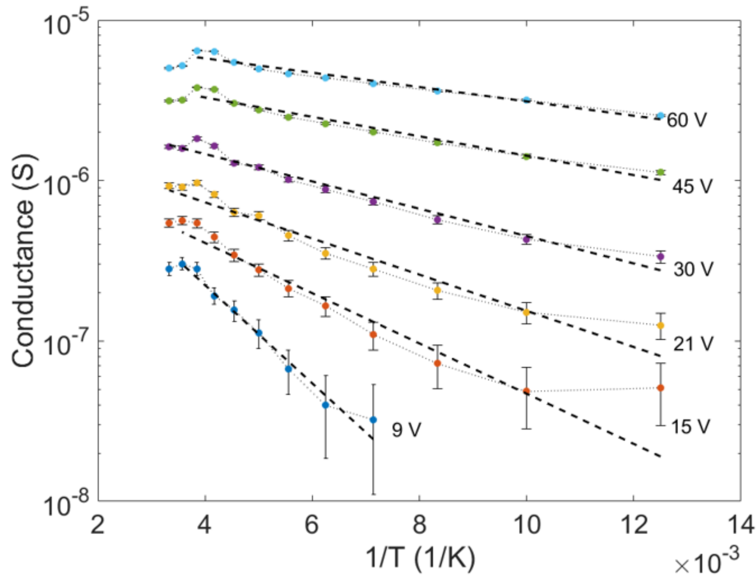


Figure 3.20: Electrical conductance as a function of temperature on an Arrhenius plot. The electrical conductivity shows activated behavior at all gate voltages

up thereby reducing the activation energy, consistent with our experimental observation.

Similar explanation has been qualitatively given in a previously published study [24]. In this study, the density of localized states was assumed to be a steep function of energy and the activation behavior has been attributed to nearest neighbor hopping. The activation energy is qualitatively described as the average energy difference between the nearest neighbors. If $N(\varepsilon_F)$ is the density of states at the Fermi level position, then the energy difference between the nearest neighbors can be roughly estimated as $1/N(\varepsilon_F)a$, where a is the average distance between the nearest neighbors. If the density of states $N(\varepsilon)$ is an increasing function of energy, then the activation energy should decrease with increasing gate voltage, as observed in the experimental data.

While the description given above seems to separate the two hypothesis as mutually exclusive processes, that is not necessarily the case. In reality, the current measured is the result of motion of electrons in the conduction band as well as the ones in the localized band tail. When the Fermi-level is in- or under the band tail, the number of electrons occupying the localized states ($n_L$) is much higher than the number of electrons occupying the extended

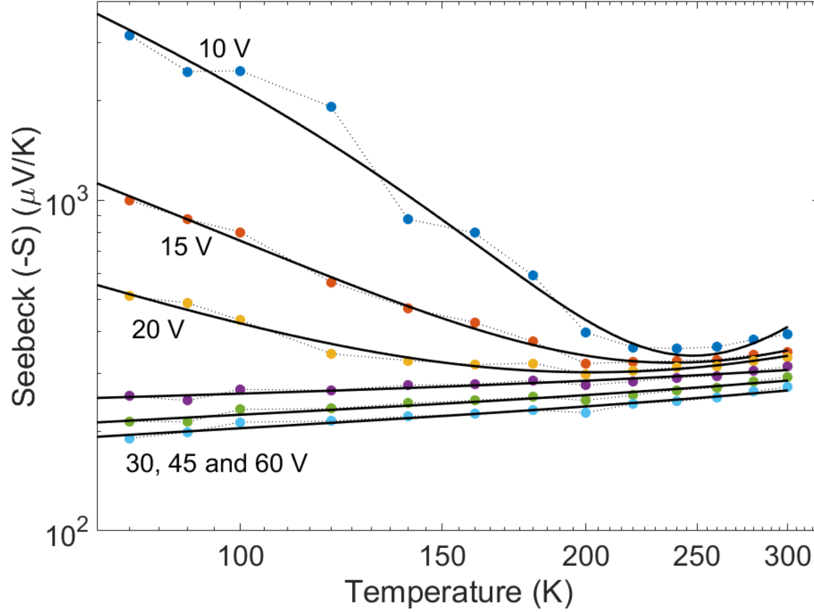


Figure 3.21: Seebeck coefficient of monolayer $MoS_2$ plotted as a function of temperature at various gate voltages. The solid lines are the fits obtained by using the Seebeck coefficient expression for transport by electrons activated to the mobility edge

states ($n_C < n_L$) in the conduction band. However, the electrons in the extended states are itinerant and have higher mobility ($\mu_E > \mu_L$) than the localized states. The mechanism which has the the higher value of $ne\mu$ will dominate the conduction mechanism.

The determination of the correct transport mechanism is not possible to make from just the electrical conductivity data. The possibility of the contributions from both the mechanisms further complicated the analysis. Measurement of Seebeck coefficient (S) could however provide an additional insight into the transport physics. The temperature dependence of the Seebeck coefficient at various gate voltages, as shown in Fig. 3.21.

An obvious observation of negative Seebeck coefficient confirms the n-type behavior of the $MoS_2$ channel. Secondly, as the gate voltage is increased, the magnitude of the Seebeck coefficient decreases at all temperatures, this is because of the upward movement of the Fermi level $\varepsilon_F$ with increasing gate voltage, thereby reducing the average entropy carried by the electrons $< \varepsilon - \varepsilon_F > /T$. As for the temperature dependence, at low gate voltages, the magnitude of the Seebeck coefficient initially decreases with increasing

| | Electrical conductivity | Seebeck Coefficient |
|---|---|---|
| Localized states<br>Purely Localized transport:<br>$C_1 + C_2T^2 = E_A - 2.5\varepsilon_t < E_A$ | $E_A \sim \varepsilon_t ln\left(\frac{v_c(\gamma kT)^2}{N(\varepsilon_F)}\right)$ | $S = -\frac{(E_A - 2\varepsilon_t)}{eT}$ |
| Extended states<br>Purely extended transport:<br>$C_1 + C_2T^2 = \varepsilon_C - \varepsilon_F = E_A$ | $E_A = \varepsilon_C - \varepsilon_F$ | $S = -\left(\frac{\varepsilon_C - \varepsilon_F}{eT} + A\right)$<br>$\varepsilon_F = \varepsilon_{F,0} - \varepsilon_F'' T^2$ |
| | $\boldsymbol{\sigma = \sigma_0 exp(-E_A/kT)}$ | $\boldsymbol{S = -\frac{C_1}{eT} - \frac{C_2T}{e} + C_3}$ |

Figure 3.22: Summary of theoretical expressions for electrical conductivity and the Seebeck coefficient when localized and extended states are considered in isolation

temperatures and then increases marginally at around 200 K. This is a novel observation compared to what has been reported for the exfoliated films [25] as well as for the CVD grown films [30]. At higher gate voltages, the Seebeck coefficient increases monotonically with temperature which is commonly observed in highly doped semiconductors/metals where the charge transport happens by the diffusion of electrons occupying extended states. This observed temperature variation of Seebeck coefficient can be used to obtain further insight into the electron transport mechanism. The summary of theoretical expressions given in Fig.3.22 can be used for that purpose.

In this table, the theoretical expressions for electrical conductivity and the Seebeck coefficient are provided. The expression given in the first row were derived assuming that only the localized states are present in the system and that the extended states can be ignored. Similarly, the expressions in the second row represent the case where the localized states are absent and the electrons occupy only the extended states. The ambiguity regarding the transport mechanism discussed in conjunction with the electrical conductance data can be summarized from the electrical conductivity column, with both the mechanisms giving an activated behavior. Looking at the column for the Seebeck coefficient expressions, it can be seen that both the expressions can be written as $S = -C_1/eT - C_2T/e + C_3$. In this equation, the second term $C_2T/e$ arises because of the statistical shift of Fermi-level with

temperature. As seen in the 3.21, this expression fits the experimentally measured Seebeck data really well. The fitting parameters $C_1$, $C_2$ and $C_3$ can now be used to discuss the ambiguity in transport mechanism.

If electrons in the extended states dominate both the current and entropy flow, the expression $C_1 + C_2T^2$ from the Seebeck coefficient fitting should match the activation energy obtained from the electrical conductance data. For similar considerations for the localized states, the expression $C_1 + C_2T^2$ should be smaller than the activation energy obtained from the electrical conductance by $2\varepsilon_t$. In Fig.3.23, the activation energies from the electrical conductance data and the expression $C_1 + C_2T^2$ from the Seebeck data fitting are plotted together. It can be seen from the figure that in contrast to the above discussed theoretical expectations, the electrical conductance activation energy is smaller than $C_1 + C_2T^2$. So, it can be inferred that the charge transport and the entropy transport cannot be explained by considering just the localized states, or just the extended states. In other words, there is a mismatch in the mechanism that dominates the current flow and the entropy flow. The fact that the Seebeck "activation energy" is higher than that of the electrical conductance indicates that higher energy electrons dominate the entropy transport. Based on these inferences, the following description of the electron transport mechanism can be given. In the $MoS_2$ samples measured, the electrons in both the localized and the extended states flow from one side to another under applied non-equilibrium conditions. The non-equilibrium condition could be an electrical field or a temperature gradient. Considering the current flow under an applied electrical field, the electrons in the localized states outnumber the number of electrons in extended states, and therefore dominate the current despite being low in mobility. However, when considering the entropy flow under an applied temperature gradient, the electrons occupying the localized states near the Fermi-level contribute very little due to smaller or negative $(\varepsilon - \varepsilon_F)/T$ values. Therefore, the electrons in the extended states dominate the entropy transport.

Similar arguments regarding the transport mechanism can be made by observing the temperature variation of the Peltier coefficient $\pi = ST$. The Seebeck data is replotted as the Peltier coefficient in Fig. 3.24. It can be seen from the figure that at 15 and 20 V gating, the Peltier coefficient is nearly constant at 80 mV and 40 mV respectively at low temperatures and then transitions to an increasing as the temperature is further increased. It

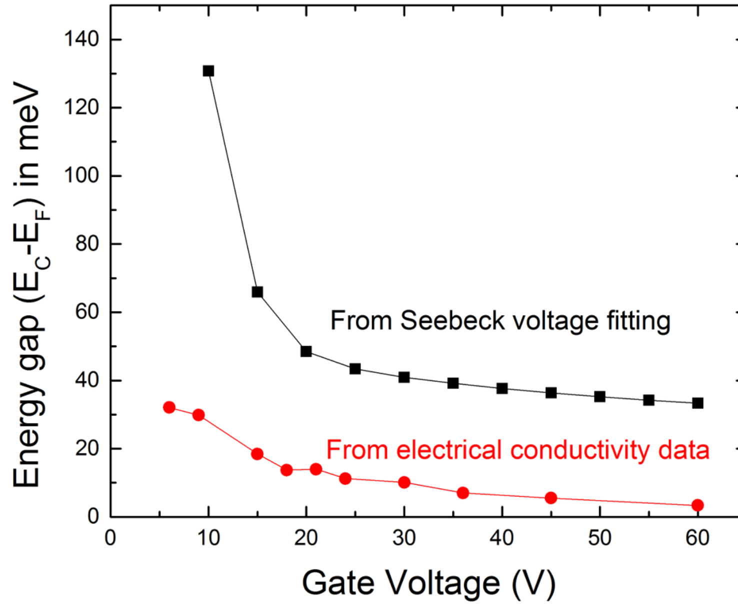


Figure 3.23: The activation energy or energy gap obtained from the Seebeck coefficient fitting and from the electrical conductance data

can also be observed that the transition temperature decreases as the gate voltage is increased. Recall that the Peltier coefficient is the average energy carried by the electrons, $< \varepsilon - \varepsilon_F >$. Considering the magnitude of the Peltier coefficient at 15 V gating, it can be said that the average energy of the electrons carrying the heat is 80 meV above the Fermi-level. This number is much higher than the activation energy of 16 meV obtained from the conductance data.

This discrepancy can be explained again as follows: Both the extended and the localized electrons carry the current. However, most of the current is carried by the localized electrons close to the Fermi-level. When accounting for the energy carried by the carriers, the localized electrons do not contribute much due to their proximity to the Fermi level. In other words, the $< \varepsilon - \varepsilon_F >$ contribution from the localized electrons is small. In fact, this contribution averages to nearly zero, if the density of states is a very slowly varying or a uniform function near the Fermi level.

The near-constant followed by the increasing trend of the Peltier coefficient can be explained by the statistical shift of the Fermi-level. As discussed

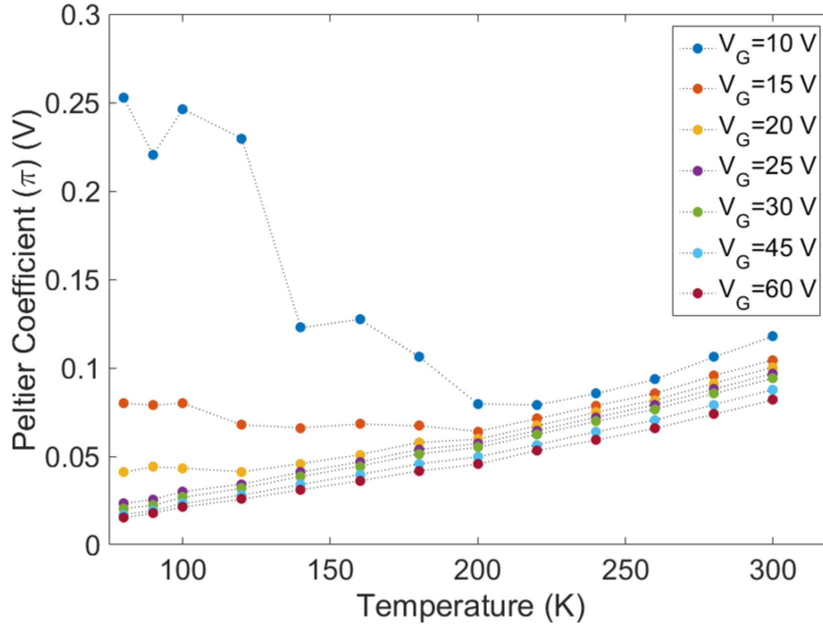


Figure 3.24: Peltier coefficient of monolayer $MoS_2$ plotted as a function of temperature at various gate voltages.

in chapter 2, as the temperature is increased, the Fermi-level shifts down resulting in a higher value of $< \varepsilon - \varepsilon_F >$. Assuming the contribution from the localized states to be zero, the shift in Fermi-level with temperature can be traced using the expression for the Peltier coefficient for semiconducting materials.

$$\pi = \frac{k_B}{e}\left(\frac{\varepsilon_C - \varepsilon_F}{k_B} + AT\right) \tag{3.13}$$

Here A is called the kinetic term and it represents the energy transported by the electrons above the conduction band edge. A is given by

$$A = \frac{\int_0^\infty \frac{\varepsilon}{k_B T}\sigma(\varepsilon)d\varepsilon}{\int_0^\infty \sigma(\varepsilon)d\varepsilon} \tag{3.14}$$

with $\varepsilon$ being measured relative to the conduction band edge energy $\varepsilon_C$. In two dimensional materials with constant density of states in the conduction band, the value of A is 1. Assuming this value to be true in Eq. 3.13, the position of the Fermi level can be traced as shown in Fig. 3.25.

We note that this calculation is an overestimation as it neglects the fi-

shift under activation assumption.png

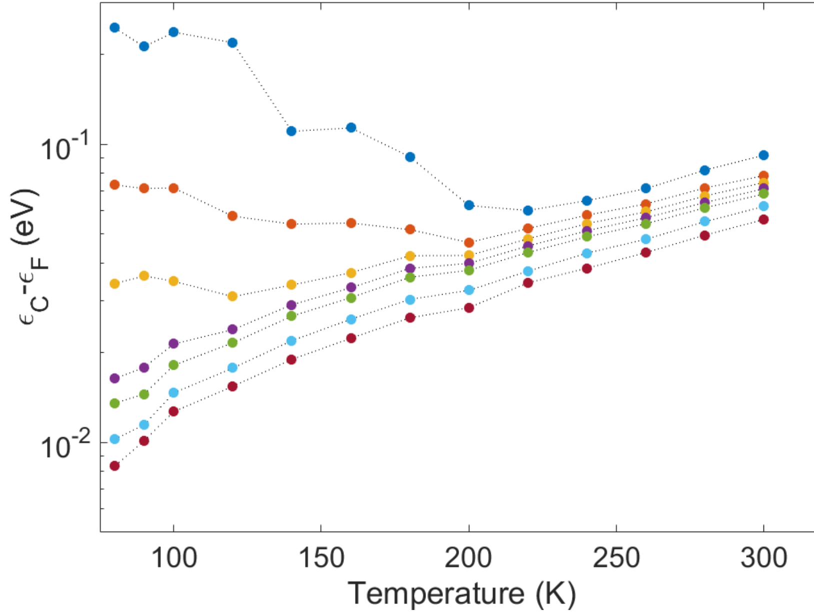


Figure 3.25: The position of Fermi level from the mobility edge calculated from the Peltier coefficient measurements. The values are positive when the Fermi-level is under the edge.

nite contribution of energy carried by the localized states. The decreasing trend at low gate voltages indicates that the Fermi-level is moving towards the mobility edge with increasing temperature. This upward movement is only possible when the carrier concentration is influenced by the activation of electrons across the Fermi-level, very similar to the intrinsic limit in silicon. This indicates the possible presence of a bump in the density of states function at around 0.25 eV from the conduction band edge.

Finally, the power factor of $MoS_2$ is plotted as a function of temperature at various gate voltages in Fig.3.26. The maximum power factor measured for the sample presented here is $1mW/K^2m$ at 60 V back gate voltage (Carrier concentration of 2.5x$10^{12}/cm^2$). We can observe from the figure that the power factor increases with increasing gate voltage at all temperatures. This indicates that the low electrical conductivity is the limiting factor in applicability of $MoS_2$ in thermoelectric applications. This inference can be further consolidated by comparing the experimentally obtained Seebeck and electrical conductivity values with corresponding predictions from the semi-classical calculations [1]. The maximum power factor observed ex-

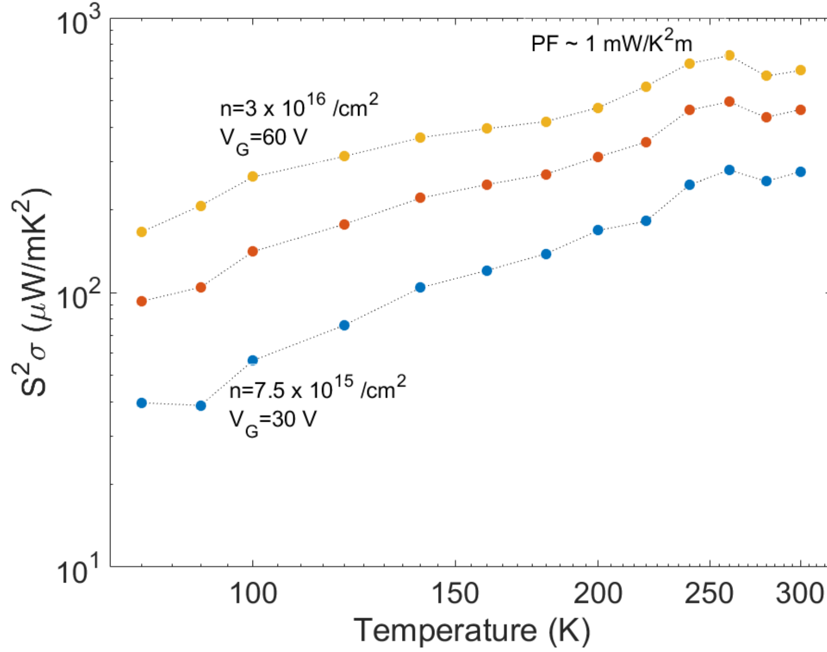


Figure 3.26: Power factor $S^2\sigma$ of monolayer $MoS_2$ plotted as a function of temperature at various gate voltages.

perimentally is smaller than the theoretical prediction by a factor of 20 at the same carrier concentration (60 V gating). Under these conditions, the experimentally observed Seebeck coefficient and the electrical conductivity are 280 $\mu V/K$ and 6000 S/m respectively. Corresponding values from the semi-classical calculation are 450 $\mu V/K$ and $10^5$ S/m. While the Seebeck coefficient is smaller by a factor of 1.5, the electrical conductivity is smaller by a factor of 15. Therefore, for successful use of $MoS_2$ in thermoelectric applications, the electrical conductivity needs to be improved, perhaps by doping methods or by decreasing the trap states.

## 3.5 Conclusion

In conclusion, AC and DC measurement techniques for thermoelectric characterization of 2D transition metal dichalcogenides are presented. Due to high channel impedance in 2D materials, DC methods with high input impedance instruments are preferable to AC methods. However, care must be taken to prevent many possible offset errors in the DC methods.

The electrical conductance and the Seebeck coefficient measured by the described DC methods are also shown. The measured electrical conductance shows an activated behavior at all gate voltages. Two plausible hypotheses are presented to explain the observed electrical conductance data. Using the Seebeck coefficient data and its fitting, the ambiguity in the electrical conductance data has been resolved and an overall picture of electron transport has been presented.

It has been concluded from the analysis that the electrons in both the extended and the localized states contribute to the charge and the entropy flow. However, the charge transport is dominated by the localized electrons while the entropy transport is dominated by the electrons in the extended states. Finally, a maximum power factor of nearly $1mW/K^2m$ has been observed which is comparable to the power factor of $5mW/K^2m$ in $Bi_2Te_3$. By comparing the observed power factor with the semi-classical calculations, it has been shown that the lower electrical conductivity in real $MoS_2$ samples limits its applicability in thermoelectric devices.

# CHAPTER 4

# THERMAL CONDUCTIVITY MEASUREMENT OF 1D STRUCTURES

## 4.1 Introduction

One dimensional structures like nanowires are promising thermoelectric materials as they exhibit lower thermal conductivity values compared to their bulk counterparts. Understanding phonon transport in these structures can help in engineering them so as to push their thermal conductivities even lower. Thermal conductivity measurement using the suspended bridge MEMS platform [52],like the one shown in Fig 4.1, is a powerful method often used to gain such fundamental insight into phonon transport in 1D structures.

For example, this platform has been used successfully to advance the understanding of phonon transport in silicon nanowires for thermoelectric applications. Initially, the platform was used to show [53] that silicon's thermal conductivity reduces from 150 W/mK in bulk to 40 W/mK in nanowires. A further reduction in thermal conductivity was hypothesized [54] for nanowires with rough surfaces based on experiments done using a similar platform. Our group and others carried out systemic measurements [12] of the thermal conductivity of silicon nanowires for various surface roughness profiles to test this hypothesis. Using multiple scattering theory [55], we demonstrated that the thermal conductivity can indeed be reduced by roughening the nanowires such that the roughness correlation length is comparable to the wavelength of the dominant phonon mode.

It is apparent from the above example that this measurement technique is an effective way to understand the influence of microstructure engineering on phonon transport. The benefits of this technique can be further advanced and used for much more sensitive measurements if certain limitations could be addressed. In this chapter, we describe the measurement principal and the limitations of this technique. We then provide a description of the solutions

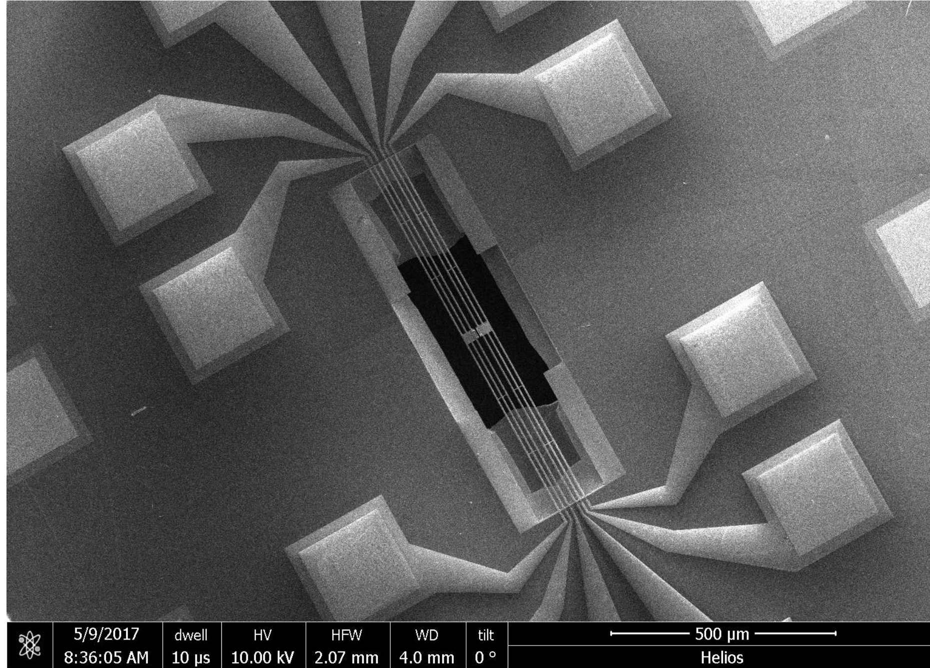


Figure 4.1: Scanning electron microscopy image of the suspended bridge platform used to measure thermal conductivity of one-dimensional structures

developed by our group and others to address these limitations, along with the results of the implementation of these solutions in our lab.

## 4.2 Measurement Principle

Fig.4.2 shows a higher magnification scanning electron microscope image of Fig. 4.1. Using these two figures, it can be seen that the device includes two suspended membranes, each supported by six long, thermally resistive silicon nitride ($SiN_x$) beams. These membranes are designated as heating (H) and sensing (S) membranes. Each membrane has a 30nm thick platinum (Pt) serpentine coil sandwiched between two $SiN_x$ films [12] that serve as resistive heaters/thermometers. The platinum coils (with electrical resistances $R_H$ and $R_S$) are connected to the contact pads via Pt leads (resistance $R_L$ each) that run through the supporting beams. The 1D structure to be measured is placed between the heating and sensing membranes and the entire device is kept at bath temperature $T_0$ in a high-vacuum cryostat.

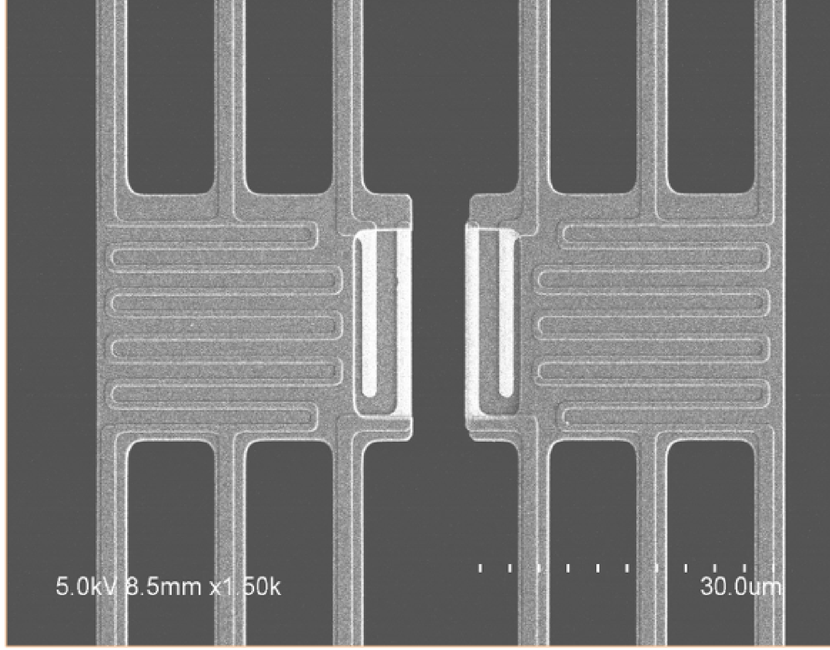


Figure 4.2: Higher magnification SEM image of the heating and sensing membranes at the center of the device shown in Fig. 4.1. The sample to be measured is placed across the membranes

Once the entire device equilibrates to its bath temperature $T_0$, DC current ($I$) is passed through the Pt coil in the heating membrane. Joule heat is generated in the coil ($QH = I^2R_H$) and two of the leads ($2Q_L = 2I^2R_L$) connecting the coil to the contact pads. Half of the heat generated in the leads reaches the membrane and the other half flows to the substrate at temperature $T_0$. The total heat in the heating membrane $Q_H + Q_L$ now flows to the substrate at $T_0$ through two pathways. One pathway is directly through the six beams supporting the heating membrane at temperature $T_H$. This pathway is represented by the lower branch of the thermal circuit in Figure 4.3. The upper branch in the thermal circuit represents the second heat conduction pathway and it includes the sample, the sensing membrane at temperature $T_S$ and its beams.

By conservation of energy, the heat flowing through the first pathway $Q_1 = G_B(T_H - T_0)$ and the second pathway $Q_2 = G_B(T_S - T_0)$ add up to the total heat in the heating membrane $Q_H + Q_L$. Assuming the thermal conductance of the beams supporting the heating and the sensing membranes to be equal ($G_B$), the thermal conductance of the beams is

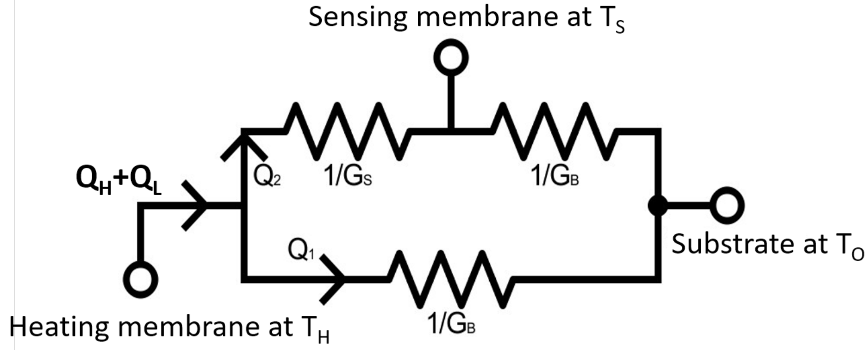


Figure 4.3: Thermal circuit representing the heat flow pathways from the heating memebrane at temperature $T_H$ to the substrate at temperature $T_0$

$$G_B = \frac{(Q_H + Q_L)}{((T_H - T_0) + (T_S - T_0))} \tag{4.1}$$

Finally, the heat flowing through the sample $G_S(T_H - T_S)$ is same as the heat flowing between the sensing membrane and the substrate $G_B(T_S - T_0)$. This yields the sample conductance $G_S$ as

$$G_S = G_B \frac{(T_S - T_0)}{(T_H - T_S)} \tag{4.2}$$

The steady state temperatures, $T_H$ and $T_S$, of the two membranes are obtained by measuring the coil resistances, $R_H$ and $R_S$. The heat flowing through the heating membrane $Q_H + Q_L$ is obtained as $(R_H + R_L)I^2$ by measuring $R_H + R_L$. To measure these resistances, small AC currents at different frequencies are passed through the coils on the heating and sensing sides, and the corresponding voltage drops measured using lock-in amplifiers [52]. The resistance data can then be converted to a temperature rise using the calibration curve for $R_H$ and $R_S$. Figure 4.4 shows a typical temperature rise measurement as the DC heating current $I$ is swept.

The sample conductance obtained using this device includes the contact conductance between the membranes and the sample. Care should be taken to minimize this contact resistance by welding the sample to the membranes. This is achieved with a large platinum patch deposited using e-beam induced deposition in a focused ion beam tool.

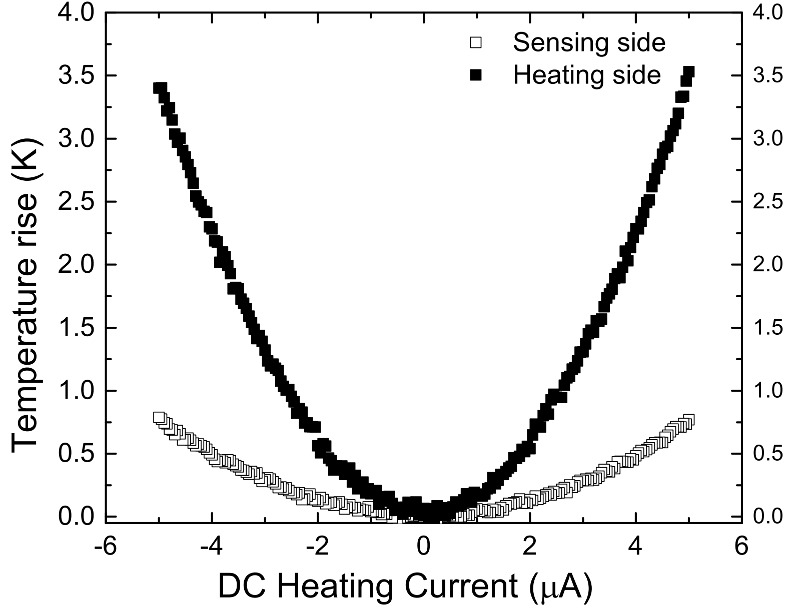


Figure 4.4: Temperature rise on heating ($T_H - T_0$) and sensing ($T_S - T_0$) sides as the DC heating current is swept

## 4.3 Limitations and solutions

In this section, we list the limitations of the measurement technique as described so far.

### 4.3.1 Sample mismatch between measurement and imaging

Consider the thermal conductivity measurement of a 1D structure like a nanowire. The nanowire to be measured is placed across the membranes using a drop casting method or by using an omniprobe in a focused ion beam (FIB) tool. Drop casting method is easier of the two methods as it just involves placing a drop of isopropyl alcohol with nanowires suspended in it on the measurement platform. However, in this method, it is very challenging to characterize the microstructure of the same wire that has been measured. Nanowires taken from the same suspension are used to characterize the microstructure and are assumed to represent the actual nanowire measured. This assumption introduces an uncertainty in the study of influence of mi-

crostructure on phonon transport.

In the omniprobe method, a wire placed on a holey carbon carbon grid is first characterized for its roughness or other microstructure information under a transmission electron microscope (TEM). The same wire is then transferred using an omniprobe from the carbon TEM grid onto the measurement platform. This method is laborious and includes the risk of damage to the nanowire by gallium ions used in the transfer process. The impact of the ion irradiation is exacerbated when dealing with ultrafine wires.

To overcome the problems associated with the above two processes described, we modified the fabrication of the measurement platform so that there is a through hole underneath the membranes as shown already in Fig. 4.1. The through hole enables direct TEM imaging and thermal conductivity measurement of the same 1D structure while also allowing the use of the easier drop casting method. The modified platform can be also be used to perform in-situ measurement of thermoelectric properties under various conditions like applied strain etc.

To fabricate the through holes under the membranes, we start with a lightly doped 300 $\mu m$ thick 4 inch silicon wafer. We protect the front side of the wafer with a film stack of 30nm/30nm/300nm PECVD $SiN_x/SiO_2/SiN_x$. we then deposit 350 nm of PECVD $SiN_2$ on the back side of the wafer. Using photolithography (EVG 620 mask aligner) and $CF_4$ Freon reactive ion etching (RIE), we pattern $700\mu m$ x $700\mu m$ windows through the $SiN_x$ deposited on the back side. Using 20 wt% potassium hydroxide (KOH) solution for 90 minutes, we etch around 90 $\mu m$ of silicon through the windows on the back side of the wafer. The protective stack on the front side is then etched away using a combination of Freon RIE etching and buffered oxide etch (BOE). Using one backside alignment and two front side alignment steps, we pattern the Pt lines and beams on the front side of the wafer as usual [52]. During the final step of suspending the membranes, the KOH etches silicon from both top and bottom side of the wafer resulting in a through hole.

The fabricated devices are 1cm x 1cm in size and do not fit inside the conventional TEM holder used for $3mm$ x $3mm$ TEM grid. To overcome this problem, we use an in-house built Beryllium copper TEM holder, shown in Fig. 4.5a. The holder is designed to accommodate the 1cm x 1cm device chips and to align the through hole in our devices to the beam path in the TEM. The alignment is apparent from Fig 4.5b which is a picture of the

TEM phosphor screen taken as soon as the holder was inserted.

### 4.3.2 Measurement accuracy

It follows from the above discussion that the combination of the modified thermal conductivity measurement platform and the associated imaging capability opens the door to undertake more precise thermal measurements. One possibility is the measurement of thermal conductivity of ultra-fine nanowires. Another possibility is to measure thermal conductivities of samples with subtle differences in their microstructure. Yet another possibility is to modify the platform to apply strain on the sample and measure corresponding changes in the thermal conductivity. Since the changes in the microstructure can be characterized precisely, valuable information regarding the correlation between the material's microstructure and its thermal properties can be obtained.

Limitations in the accuracy and resolution of the thermal conductance measurement hamper the implementation of the possibilities listed above. Accuracy of the measurement is limited by presence of stray thermal conductance resulting from the radiative and convective heat transfer between the membranes. These contributions become important and must be accounted for while performing measurements on samples with very small thermal conductances. To estimate the thermal conductance contribution from stray heat transfer sources, we performed the measurement on an empty device without any 1D structure across the membranes. Fig.4.6 shows measured stray thermal conductances at room temperature and above. At room temperature, the stray conductance is just over 600 pW/K. Therefore, it is necessary to experimentally estimate the stray conductance while performing measurements on ultra-thin samples with conductances of the order of 1 nW/K.

We expect the stray conductance to vary from one device to another. So, the stray conductance must be measured on the same platform on which the 1D structure is measured. This can be done by cutting the 1D structure in an FIB tool after the measurement. Alternatively, the measurement on the empty device can be done before the 1D sample is transferred onto the platform. We also note that the heat transfer contribution due to convection can be minimized by maintaining high levels of vacuum in the cryostat.

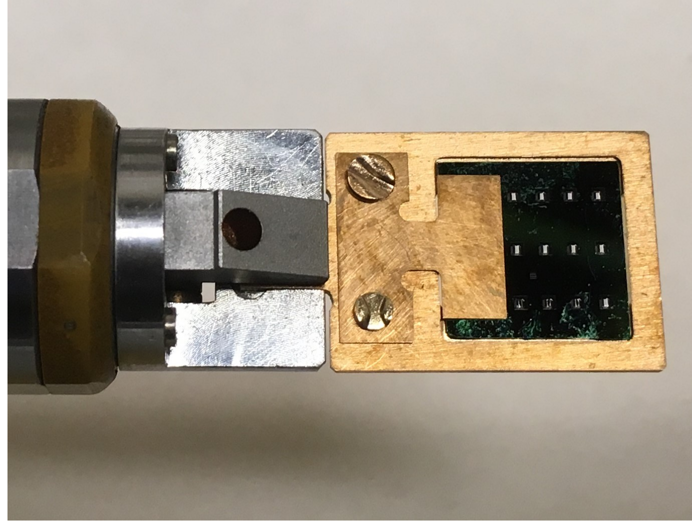

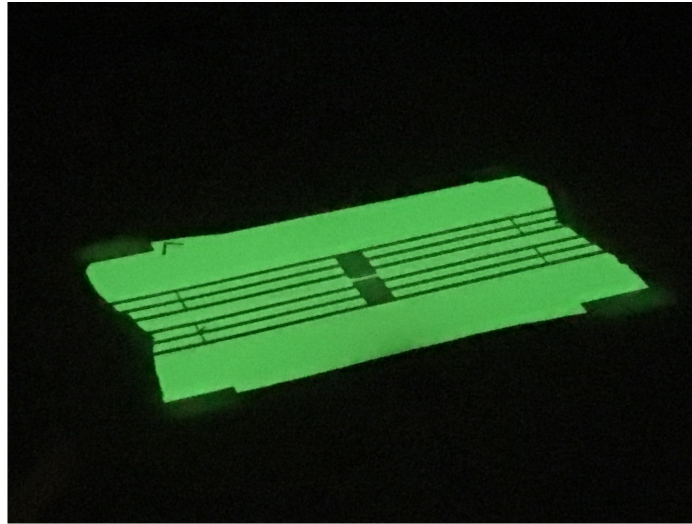

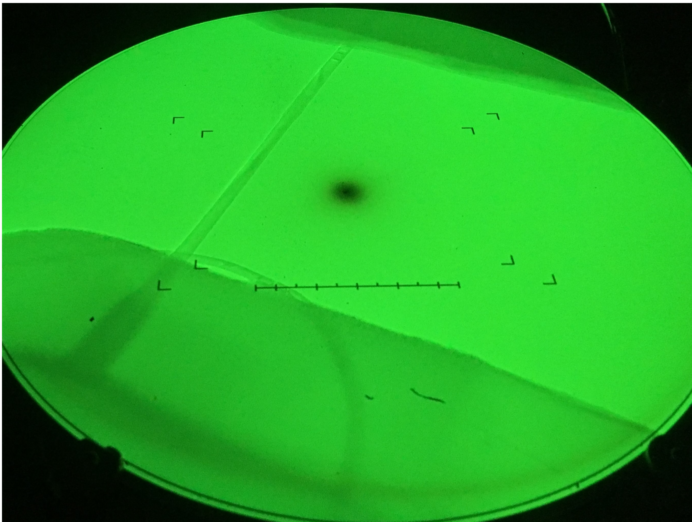

Figure 4.5: Images of the in-house biult transmission electron microscope holder that can accommodate the thermal conductivity measurement platform and align it to the electron beam inside a TEM

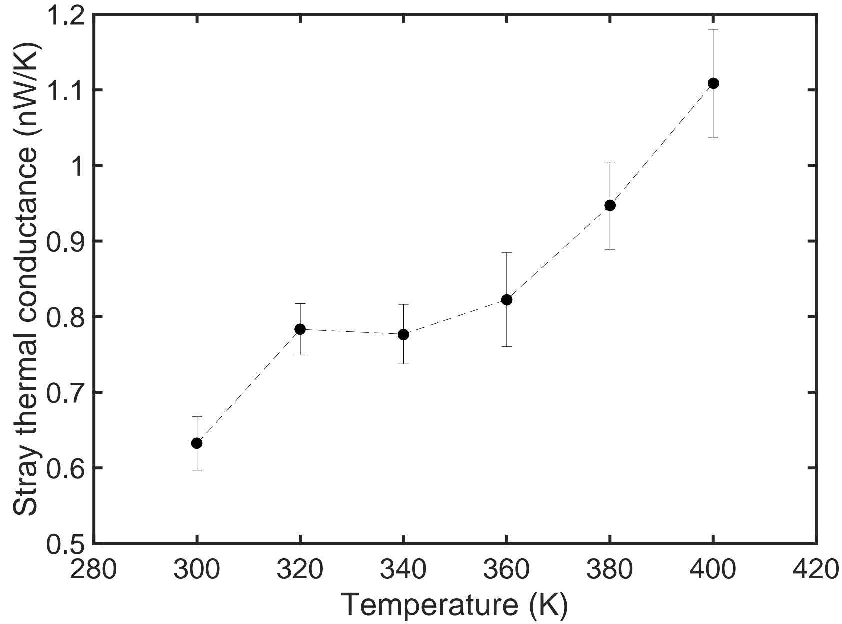


Figure 4.6: Thermal conductance measured on a platform without any sample across the membranes. The measured conductance is the result of radiative and convective heat transfer between the membranes

This measurement shows that thermal conductances as small as 500 pW/K can be measured using the current measurement platform and instrumentation. This number does not represent the smallest conductance that can be measured. The lower measurement limit can be pushed further down by making the platinum resistance coils more resistive as long as the stray conductances are accounted for.

Another source of systemic error is caused by the asymmetry of the measurement platform, as suggested in ref. [14]. In the measurement principal described in the previous section, it was assumed that the thermal conductances of the six beams on the heating and the sensing side were equal. In other words, referring to Fig.4.3, $1/G_B$ thermal resistance is assumed to be same in the top and the bottom branch. However, in a real platform, the beams do not have the exact same thermal conductance on both the sides. While the difference is typically small, it follows from Eq.4.2 that it could result in error depending on the temperature rise on the sensing side. For example, if the temperature rise on the heating and the sensing side are 5 K and 1 K respectively, a 1 nW/K error in beam conductance $1/G_B$ can

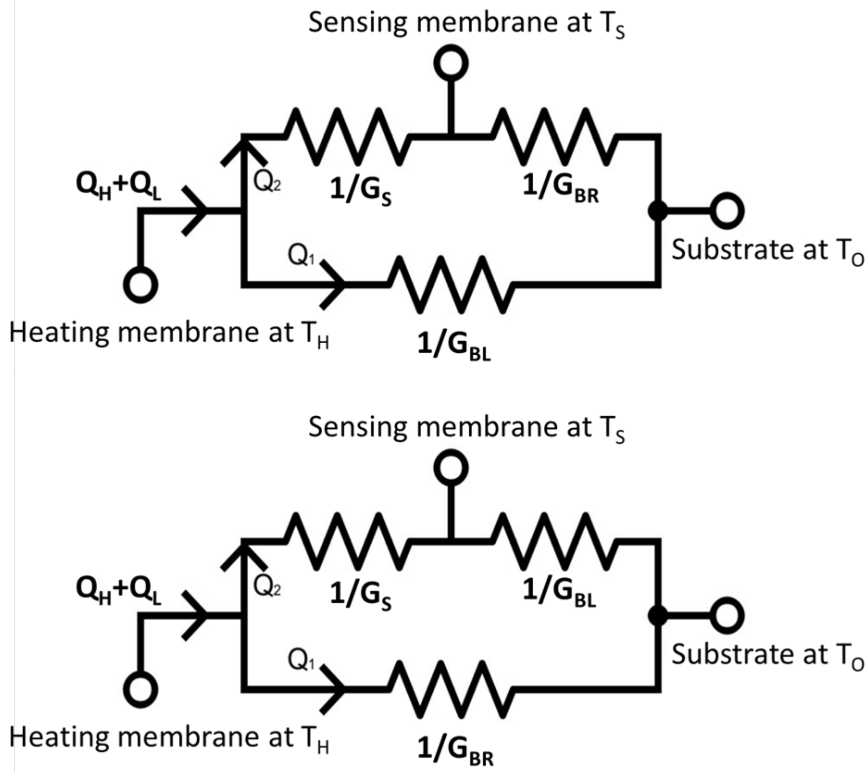


Figure 4.7: Thermal circuits representing the measurement scheme that accounts for asymmetry in thermal conductance of the beams on the heating and the sensing side

cause an error of the order of 250 pW/K. Note that this error is minimized while working with samples with lower conductances because of the lower temperature rise $(T_S - T_0)$ on the sensing side. As a result, this is not a critical error contribution for ultra-thin nanowires. It's contribution can be further reduced by making the beams more resistive, perhaps by using four beams on each side instead of six. In the following paragraphs, we describe a simple method [14] that could be used to estimate this error contribution.

The asymmetry in beam thermal conductance can be taken into account by switching the heating and sensing membranes and repeating the experiment. Corresponding thermal circuits for the analysis are shown in Fig. 4.8. The figure on the top is for measurement where the left hand side membrane is used as the heating side. The reverse case is represented by the bottom figure. In the figure, $1/G_{BL}$ and $1/G_{BR}$ represent the thermal conductances of the left and the right side beams respectively.

Applying conservation of energy at node $T_H$ in both the circuits, the following equations can be written:

$$\begin{aligned} Q_{LR} &= (T_S - T_0)_{LR} G_{BR} + (T_H - T_0)_{LR} G_{BL} \\ Q_{RL} &= (T_S - T_0)_{RL} G_{BL} + (T_H - T_0)_{RL} G_{BR} \end{aligned} \tag{4.3}$$

The subscript LR represents the measurement in which left side membrane is the heating membrane, and vice versa. These equations can be rewritten as:

$$\begin{aligned} &\left(\frac{d(T_S - T_0)}{dQ}\right)_{LR} G_{BR} + \left(\frac{d(T_H - T_0)}{dQ}\right)_{LR} G_{BL} = 1 \\ &\left(\frac{d(T_S - T_0)}{dQ}\right)_{RL} G_{BL} + \left(\frac{d(T_H - T_0)}{dQ}\right)_{RL} G_{BR} = 1 \end{aligned} \tag{4.4}$$

The terms in the brackets are obtained as slopes from corresponding plots. Solving the pair of equations, we get the thermal conductances of the beams on the left and the right side.

From the figure, it can be seen that the beams differ in their thermal conductance by $\sim$ 1nW/K. The maximum temperature rise on the heating and the sensing side for the sample measured were 4.1 and 1.3 K respectively. These numbers imply that platform asymmetry causes an error of $\sim$ 0.5 nW/K. The sample measured had a room temperature thermal conductance of 20 nW/K. For a 1nW/K sample, the error would be 25 pW/K.

## 4.4 Conclusions

In this chapter, we pointed out various limitations in the suspended bridge measurement platform and present the solution to eliminate or estimate the impact of these limitations. The most important limitation is the mismatch between the sample that is measured and the one that is characterized. This introduces a major uncertainty in correlations between material's microstructure and phonon transport. This limitation is eliminated using a transmission electron microscope holder that can accommodate and align the measurement

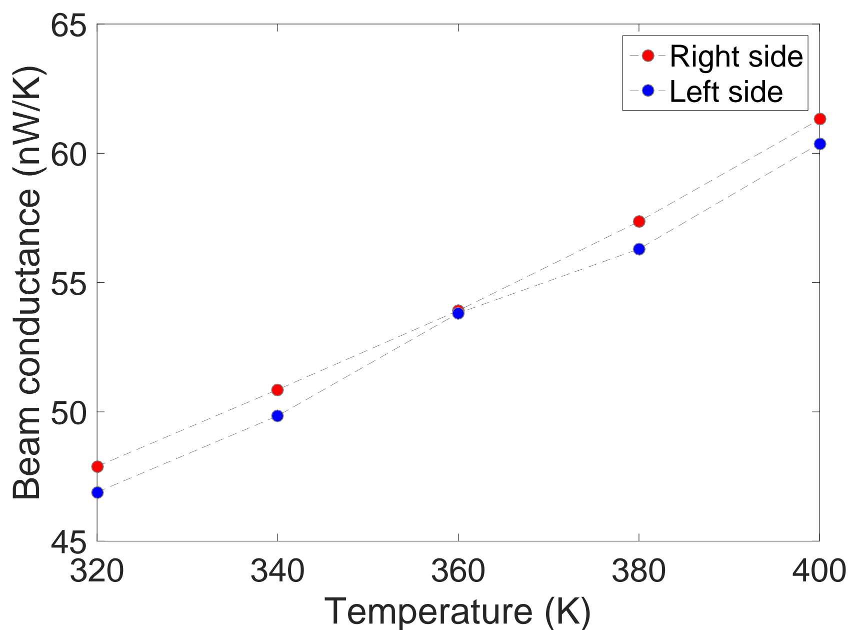


Figure 4.8: Thermal conductance of the beams on the left and right side of the measurement platform. The difference is of the order of 1nW/K

platform to the electron beam in the TEM.

The second limitation is the measurement accuracy of the measurement platform which limits its applicability for ultra-sensitive thermal conductance measurements. We estimated this uncertainty to be of the order of 500 pW/K. This estimate is obtained by measuring the thermal conductance due of an empty device without any sample bridging the suspended membranes. This measurement of the stray conductance also indicates that the platform is sensitive to measure samples with conductances of the order of 500 pW/K. Finally, the impact of the asymmetry of the beams on the measured sample conductance and the method to estimate it is discussed.

# CHAPTER 5

# CONCLUSION AND FUTURE WORK

Our investigation of the thermoelectric properties of one- and two dimensional structures has been presented in this dissertation. For the study on two dimensional materials, we focus on the measurement of Seebeck coefficient and electrical conductivity of monolayers of Molybdenum disulphide ($MoS_2$). We observe a maximum power factor of $1mW/K^2m$ from our measurements on chemical vapor deposition grown $MoS_2$ monolayers. The power factor number is promising when compared to the power factor of $5mW/K^2m$ in $Bi_2Te_3$ which is a common material of choice in commercial thermoelectric devices. However, the maximum power factor value quoted here was observed at very high gating voltages (60 V). In our experiments, as the gate voltage is increased, we observe a decreasing Seebeck coefficient (S) due to movement of the Fermi-level closer to the conduction band edge. This observation is accompanied by increasing electrical conductivity ($\sigma$) due to increased carrier concentration. In light of these two observations and the monotonically increasing power factor ($S^2\sigma$) with increasing gate voltage, we conclude that the low electrical conductivity is the limiting factor in application of $MoS_2$ in thermoelectric applications. Since gate voltages cannot be applied in practical thermoelectric devices, doping methods need to be developed to increase the electrical conductivity of $MoS_2$ for its successful deployment in thermoelectric applications.

Apart from testing the applicability of $MoS_2$ in thermoelectric devices, this dissertation also presents crucial insights into the nature of electron transport process in $MoS_2$ monolayers. We obtain these insights by using our experimental data in combination with a theoretical framework developed in this dissertation. The theoretical framework is based on a percolation theory model that has been previously used to derive the expressions for the Seebeck coefficient and electrical conductivity in 3D materials. We derive relevant expressions for 2D materials in this dissertation assuming step function and

exponential function density of states. The theoretical structure developed in this dissertation could be used as a framework for analyzing hundreds of other 2D materials that belong to the category of transition metal dichalcogenides.

Using the theoretical framework and the experimentally observed thermoelectric properties of $MoS_2$, we show that the electrons in both the localized as well as the extended states contribute to the current and entropy transfer process. However, our analysis indicates that the electrons occupying the localized states dominate the current flow while the electrons in the extended states dominate the entropy flow or the Seebeck coefficient. The domination of the localized electrons in the charge transport process can be attributed to higher occupancy of the localized states. On the other hand, the domination of the extended electrons in the entropy transport process can be explained by considering small or negative entropy contribution of localized states due to their proximity to the Fermi level.

Further insights into the transport properties of $MoS_2$ can be obtained by extending the experiments presented in this dissertation. One immediate direction is to study the influence of the substrate and encapsulation. In our experimental studies, we observed deterioration of $MoS_2$ over time. We suspect that this is the result of oxidation of Molybdenum atoms when exposed to ambient air. A systemic study of the variation of thermoelectric properties with aging of the samples can be performed for bare and encapsulated $MoS_2$ channels. Boron nitride is a commonly used insulator for encapsulating the $MoS_2$ channel to protect it from environmental effects [56]. Due to the absence of dangling bonds, h-BN is also likely to increase the mobility of $MoS_2$ channel thereby increasing the power factor of $MoS_2$.

Another possible future direction for this work is to study the influence of intentionally introduced dopants/defects. Following the theoretical study of Mahan and Sofo [57], dopants could be introduced such that a delta function shaped density of states is formed in the band gap. By controlling the location and the intensity of the peak, the transport properties of $MoS_2$ can be controlled. Measuring the thermoelectric properties of $MoS_2$ under various gas environments could also provide different density of states in the band-gap resulting in different thermoelectric properties.

As for the one dimensional materials, the focus of the dissertation is on the measurement of thermal conductivity using a suspended bridge platform. More specifically, the focus is on removing certain limitations of the

measurement platform that hinder its applicability for samples with very low thermal conductances. In our earlier measurements on silicon nanowires using the platform, one of the biggest limitations was the mismatch between the sample that was measured and the one that was characterized. In order to carryout thermal measurement and microstructure characterization on the same 1D sample, we modified the fabrication procedure to introduce a through hole underneath the device platform. Additionally, we custom built a TEM holder that can accommodate the 1cm x 1cm device chips and also align the device platform along the electron beam in a TEM.

We also estimated the stray thermal conductance as a result of radiation and convection between the two membranes to be of the order of 500 pW/K. This establishes that while measuring samples with thermal conductance of the order of 1 nW/K, the stray thermal conductance of the platform must be characterized. The impact of the device asymmetry for samples of high and low thermal conductances is discussed and a method to estimate this error is provided.

The measurement platform can be improved in several different ways and can to include several features. A first step would be to fabricate the samples with four supporting beams instead of six on heating side. This will result in an more heat to flow through the sample and the sensing side beams, resulting in higher temperature rise on the sensing side. Such a feature will be beneficial for measuring thermal conductance of samples with very low thermal conductance. Furthermore, the beams on the sensing side could be made wider to increase their thermal conductance to further amplify the temperature rise on the sensing membrane. The error estimation scheme provided in this dissertation could be used to estimate the beam asymmetry could be used to easily extract thermal conductance of the samples.

With the TEM characterization capability on the measurement platform, new dimensions could be added to the platform. In-situ thermal conductivity measurements can be carried out to study phonon transport as a function of applied stress [58] or under different ambient conditions.

# REFERENCES


[1] H. Babaei, J. M. Khodadadi, and S. Sinha, "Large theoretical thermoelectric power factor of suspended single-layer mos2," *Applied Physics Letters*, vol. 105, no. 19, p. 193901, 2014. [Online]. Available: http://dx.doi.org/10.1063/1.4901342

[2] C. B. Vining, "Semiconductors are cool," *Nature*, vol. 413, no. 6856, pp. 577–578, Oct. 2001. [Online]. Available: http://dx.doi.org/10.1038/35098159

[3] "Estimated u.s energy consumptoin in 2016," 2016, Lawrence Livermore national laboratory. [Online]. Available: https://flowcharts.llnl.gov/content/assets/images/charts/Energy/Energy_2016_United-States.png

[4] R. R. Heikes and R. W. Ure, *Thermoelectricity: science and engineering*. Interscience Publishers, 1961.

[5] J. P. Heremans, M. S. Dresselhaus, L. E. Bell, and D. T. Morelli, "When thermoelectrics reached the nanoscale," *Nat Nano*, vol. 8, no. 7, pp. 471–473, July 2013. [Online]. Available: http://dx.doi.org/10.1038/nnano.2013.129

[6] I. Chowdhury, R. Prasher, K. Lofgreen, G. Chrysler, S. Narasimhan, R. Mahajan, D. Koester, R. Alley, and R. Venkatasubramanian, "On-chip cooling by superlattice-based thin-film thermoelectrics," *Nat Nano*, vol. 4, no. 4, pp. 235–238, Apr. 2009. [Online]. Available: http://dx.doi.org/10.1038/nnano.2008.417

[7] H. J. Goldsmid and R. W. Douglas, "The use of semiconductors in thermoelectric refrigeration," *British Journal of Applied Physics*, vol. 5, no. 11, p. 386, 1954. [Online]. Available: http://stacks.iop.org/0508-3443/5/i=11/a=303

[8] C. B. Vining, "The thermoelectric limit zt= 1: Fact or artifact.." in *Proceedings of the XIth Intl. Conference on Thermoelectrics, Univ. of Texas, Arlington, TX*, 1992, pp. 223–231.

[9] L. D. Hicks and M. S. Dresselhaus, "Thermoelectric figure of merit of a one-dimensional conductor," *Phys. Rev. B*, vol. 47, pp. 16 631–16 634, Jun 1993. [Online]. Available: https://link.aps.org/doi/10.1103/PhysRevB.47.16631

[10] L. D. Hicks and M. S. Dresselhaus, "Effect of quantum-well structures on the thermoelectric figure of merit," *Phys. Rev. B*, vol. 47, pp. 12 727–12 731, May 1993. [Online]. Available: https://link.aps.org/doi/10.1103/PhysRevB.47.12727

[11] A. Majumdar, "Thermoelectricity in semiconductor nanostructures," *Science*, vol. 303, no. 5659, pp. 777–778, 2004. [Online]. Available: http://science.sciencemag.org/content/303/5659/777

[12] M. G. Ghossoub, K. V. Valavala, M. Seong, B. Azeredo, K. Hsu, J. S. Sadhu, P. K. Singh, and S. Sinha, "Spectral phonon scattering from sub-10 nm surface roughness wavelengths in metal-assisted chemically etched si nanowires," *Nano Letters*, vol. 13, no. 4, pp. 1564–1571, 2013, pMID: 23464810. [Online]. Available: http://dx.doi.org/10.1021/nl3047392

[13] M. C. Wingert, Z. C. Y. Chen, S. Kwon, J. Xiang, and R. Chen, "Ultra-sensitive thermal conductance measurement of one-dimensional nanostructures enhanced by differential bridge," *Review of Scientific Instruments*, vol. 83, no. 2, p. 024901, 2012. [Online]. Available: http://dx.doi.org/10.1063/1.3681255

[14] A. Weathers, K. Bi, M. T. Pettes, and L. Shi, "Reexamination of thermal transport measurements of a low-thermal conductance nanowire with a suspended micro-device," *Review of Scientific Instruments*, vol. 84, no. 8, p. 084903, 2013. [Online]. Available: http://dx.doi.org/10.1063/1.4816647

[15] S. Sadat, E. Meyhofer, and P. Reddy, "High resolution resistive thermometry for micro/nanoscale measurements," *Review of Scientific Instruments*, vol. 83, no. 8, p. 084902, 2012. [Online]. Available: http://dx.doi.org/10.1063/1.4744963

[16] R. Venkatasubramanian, E. Siivola, T. Colpitts, and B. O'Quinn, "Thin-film thermoelectric devices with high room-temperature figures of merit," *Nature*, vol. 413, no. 6856, pp. 597–602, Oct. 2001. [Online]. Available: http://dx.doi.org/10.1038/35098012

[17] H. Böttner, G. Chen, and R. Venkatasubramanian, "Aspects of thin-film superlattice thermoelectric materials, devices, and applications," *MRS bulletin*, vol. 31, no. 03, pp. 211–217, 2006.

[18] T. C. Harman, P. J. Taylor, M. P. Walsh, and B. E. LaForge, "Quantum dot superlattice thermoelectric materials and devices," *Science*, vol. 297, no. 5590, pp. 2229–2232, 2002. [Online]. Available: http://science.sciencemag.org/content/297/5590/2229

[19] R. Mansfield and S. A. Salam, "Electrical properties of molybdenite," *Proceedings of the Physical Society. Section B*, vol. 66, no. 5, p. 377, 1953. [Online]. Available: http://stacks.iop.org/0370-1301/66/i=5/a=305

[20] K. F. Mak, C. Lee, J. Hone, J. Shan, and T. F. Heinz, "Atomically thin $\mathrm{mos}_2$: A new direct-gap semiconductor," *Phys. Rev. Lett.*, vol. 105, p. 136805, Sep 2010. [Online]. Available: https://link.aps.org/doi/10.1103/PhysRevLett.105.136805

[21] A. Splendiani, L. Sun, Y. Zhang, T. Li, J. Kim, C.-Y. Chim, G. Galli, and F. Wang, "Emerging photoluminescence in monolayer mos2," *Nano Letters*, vol. 10, no. 4, pp. 1271–1275, 2010, pMID: 20229981. [Online]. Available: http://dx.doi.org/10.1021/nl903868w

[22] H. J. Goldsmid and J. W. Sharp, "Estimation of the thermal band gap of a semiconductor from seebeck measurements," *Journal of Electronic Materials*, vol. 28, no. 7, pp. 869–872, 1999. [Online]. Available: http://dx.doi.org/10.1007/s11664-999-0211-y

[23] K. Kaasbjerg, K. S. Thygesen, and K. W. Jacobsen, "Phonon-limited mobility in $n$-type single-layer $\mathrm{mos}_2$ from first principles," *Phys. Rev. B*, vol. 85, p. 115317, Mar 2012. [Online]. Available: https://link.aps.org/doi/10.1103/PhysRevB.85.115317

[24] H. Qiu, T. Xu, Z. Wang, W. Ren, H. Nan, Z. Ni, Q. Chen, S. Yuan, F. Miao, F. Song, G. Long, Y. Shi, L. Sun, J. Wang, and X. Wang, "Hopping transport through defect-induced localized states in molybdenum disulphide," *Nature Communications*, vol. 4, p. 2642, Oct. 2013. [Online]. Available: http://dx.doi.org/10.1038/ncomms3642

[25] K. Hippalgaonkar, Y. Wang, Y. Ye, D. Y. Qiu, H. Zhu, Y. Wang, J. Moore, S. G. Louie, and X. Zhang, "High thermoelectric power factor in two-dimensional crystals of $\mathrm{Mos}_2$," *Phys. Rev. B*, vol. 95, p. 115407, Mar 2017. [Online]. Available: https://link.aps.org/doi/10.1103/PhysRevB.95.115407

[26] M. Kayyalha, J. Maassen, M. Lundstrom, L. Shi, and Y. P. Chen, "Gate-tunable and thickness-dependent electronic and thermoelectric transport in few-layer mos2," *Journal of Applied Physics*, vol. 120, no. 13, p. 134305, 2016. [Online]. Available: http://dx.doi.org/10.1063/1.4963364

[27] M. Buscema, M. Barkelid, V. Zwiller, H. S. J. van der Zant, G. A. Steele, and A. Castellanos-Gomez, "Large and tunable photothermoelectric effect in single-layer mos2," *Nano Letters*, vol. 13, no. 2, pp. 358–363, 2013, pMID: 23301811. [Online]. Available: http://dx.doi.org/10.1021/nl303321g

[28] S. Ghatak, A. N. Pal, and A. Ghosh, "Nature of electronic states in atomically thin mos2 field-effect transistors," *ACS Nano*, vol. 5, no. 10, pp. 7707–7712, 2011, pMID: 21902203. [Online]. Available: http://dx.doi.org/10.1021/nn202852j

[29] A. M. van der Zande, P. Y. Huang, D. A. Chenet, T. C. Berkelbach, Y. You, G.-H. Lee, T. F. Heinz, D. R. Reichman, D. A. Muller, and J. C. Hone, "Grains and grain boundaries in highly crystalline monolayer molybdenum disulphide," *Nat Mater*, vol. 12, no. 6, pp. 554–561, June 2013. [Online]. Available: http://dx.doi.org/10.1038/nmat3633

[30] J. Wu, H. Schmidt, K. K. Amara, X. Xu, G. Eda, and B. zyilmaz, "Large thermoelectricity via variable range hopping in chemical vapor deposition grown single-layer mos2," *Nano Letters*, vol. 14, no. 5, pp. 2730–2734, 2014, pMID: 24749833. [Online]. Available: http://dx.doi.org/10.1021/nl500666m

[31] N. F. Mott and E. A. Davis, *Electronic processes in non-crystalline materials*. OUP Oxford, 2012.

[32] N. Ashcroft and N. Mermin, *Solid State Physics*. Cengage Learning, 2011.

[33] Whall, T. E., Rigo, M. O., Jones, M. R. B., and Pointon, A. J., "The magnetite problem: The anamalous seebeck coefficient of fe3o4-xfx," *J. Phys. Colloques*, vol. 38, pp. C1–229–C1–232, 1977. [Online]. Available: https://doi.org/10.1051/jphyscol:1977148

[34] B. I. Shklovskii and A. L. Efros, *Electronic properties of doped semiconductors*. Springer Science & Business Media, 2013, vol. 45.

[35] O. Madelung, *Introduction to solid-state theory*. Springer Science & Business Media, 2012, vol. 2.

[36] A. Miller and E. Abrahams, "Impurity conduction at low concentrations," *Phys. Rev.*, vol. 120, pp. 745–755, Nov 1960. [Online]. Available: https://link.aps.org/doi/10.1103/PhysRev.120.745

[37] M. Pollak and B. Shklovskii, *Hopping transport in solids*. Elsevier, 1991, vol. 28.

[38] K. Maschke, H. Overhof, and P. Thomas, "On variable range hopping near the fermi energy. two-dimensional systems," *physica status solidi (b)*, vol. 62, no. 1, pp. 113–122, 1974. [Online]. Available: http://dx.doi.org/10.1002/pssb.2220620111

[39] I. P. Zvyagin, "On the theory of hopping transport in disordered semiconductors," *physica status solidi (b)*, vol. 58, no. 2, pp. 443–449, 1973. [Online]. Available: http://dx.doi.org/10.1002/pssb.2220580203

[40] G. E. Pike and C. H. Seager, "Percolation and conductivity: A computer study. i," *Phys. Rev. B*, vol. 10, pp. 1421–1434, Aug 1974. [Online]. Available: https://link.aps.org/doi/10.1103/PhysRevB.10.1421

[41] M. Grnewald and P. Thomas, "A hopping model for activated charge transport in amorphous silicon," *physica status solidi (b)*, vol. 94, no. 1, pp. 125–133, 1979. [Online]. Available: http://dx.doi.org/10.1002/pssb.2220940113

[42] H. Overhof, *Hopping conductivity in disordered solids*. Berlin, Heidelberg: Springer Berlin Heidelberg, 1976, pp. 239–265. [Online]. Available: http://dx.doi.org/10.1007/BFb0107746

[43] C. Gong, H. Zhang, W. Wang, L. Colombo, R. M. Wallace, and K. Cho, "Band alignment of two-dimensional transition metal dichalcogenides: Application in tunnel field effect transistors," *Applied Physics Letters*, vol. 103, no. 5, p. 053513, 2013. [Online]. Available: http://dx.doi.org/10.1063/1.4817409

[44] A. K. Geim and I. V. Grigorieva, "Van der waals heterostructures," *Nature*, vol. 499, no. 7459, pp. 419–425, July 2013. [Online]. Available: http://dx.doi.org/10.1038/nature12385

[45] C.-H. Lee, G.-H. Lee, A. M. van der Zande, W. Chen, Y. Li, M. Han, X. Cui, G. Arefe, C. Nuckolls, T. F. Heinz, J. Guo, J. Hone, and P. Kim, "Atomically thin p-n junctions with van der waals heterointerfaces," *Nat Nano*, vol. 9, no. 9, pp. 676–681, Sep. 2014. [Online]. Available: http://dx.doi.org/10.1038/nnano.2014.150

[46] Y. M. Zuev, "Nanoscale thermoelectric energy conversion," Ph.D. dissertation, Columbia University, 2011.

[47] B. M. Curtin, "Improvement and integration of silicon nanowires for thermoelectric applications," Ph.D. dissertation, University of California Santa Barabara, 2014.

[48] D. G. Cahill, "Thermal conductivity measurement from 30 to 750 k: the 3 method," *Review of Scientific Instruments*, vol. 61, no. 2, pp. 802–808, 1990. [Online]. Available: http://dx.doi.org/10.1063/1.1141498

[49] C. Dames and G. Chen, "1,2, and 3 methods for measurements of thermal properties," *Review of Scientific Instruments*, vol. 76, no. 12, p. 124902, 2005. [Online]. Available: http://dx.doi.org/10.1063/1.2130718

[50] W. Zhu, T. Low, Y.-H. Lee, H. Wang, D. B. Farmer, J. Kong, F. Xia, and P. Avouris, "Electronic transport and device prospects of monolayer molybdenum disulphide grown by chemical vapour deposition," *Nature Communications*, vol. 5, p. 3087, Jan. 2014. [Online]. Available: http://dx.doi.org/10.1038/ncomms4087

[51] K. Hess, *Advanced theory of semiconductor devices.* IEEE press, 2000.

[52] L. Shi, D. Li, C. Yu, W. Jang, D. Kim, Z. Yao, P. Kim, and A. Majumdar, "Measuring thermal and thermoelectric properties of one-dimensional nanostructures using a microfabricated device," *Journal of Heat Transfer*, vol. 125, no. 5, pp. 881–888, Sep. 2003. [Online]. Available: http://dx.doi.org/10.1115/1.1597619

[53] D. Li, Y. Wu, P. Kim, L. Shi, P. Yang, and A. Majumdar, "Thermal conductivity of individual silicon nanowires," *Applied Physics Letters*, vol. 83, no. 14, pp. 2934–2936, 2003. [Online]. Available: http://dx.doi.org/10.1063/1.1616981

[54] A. I. Hochbaum, R. Chen, R. D. Delgado, W. Liang, E. C. Garnett, M. Najarian, A. Majumdar, and P. Yang, "Enhanced thermoelectric performance of rough silicon nanowires," *Nature*, vol. 451, no. 7175, pp. 163–167, Jan. 2008. [Online]. Available: http://dx.doi.org/10.1038/nature06381

[55] J. Sadhu and S. Sinha, "Room-temperature phonon boundary scattering below the casimir limit," *Phys. Rev. B*, vol. 84, p. 115450, Sep 2011. [Online]. Available: https://link.aps.org/doi/10.1103/PhysRevB.84.115450

[56] G.-H. Lee, X. Cui, Y. D. Kim, G. Arefe, X. Zhang, C.-H. Lee, F. Ye, K. Watanabe, T. Taniguchi, P. Kim, and J. Hone, "Highly stable, dual-gated mos2 transistors encapsulated by hexagonal boron nitride with gate-controllable contact, resistance, and threshold voltage," *ACS Nano*, vol. 9, no. 7, pp. 7019–7026, 2015, pMID: 26083310. [Online]. Available: http://dx.doi.org/10.1021/acsnano.5b01341

[57] G. D. Mahan and J. O. Sofo, "The best thermoelectric," *Proceedings of the National Academy of Sciences*, vol. 93, no. 15, pp. 7436–7439, 1996. [Online]. Available: http://www.pnas.org/content/93/15/7436.abstract

[58] M. A. Haque and M. T. A. Saif, "Deformation mechanisms in free-standing nanoscale thin films: A quantitative in situ transmission electron microscope study," *Proceedings of the National Academy of Sciences of the United States of America*, vol. 101, no. 17, pp. 6335–6340, 2004. [Online]. Available: http://www.pnas.org/content/101/17/6335.abstract